Nano Research

ISSN 1998-0124 CN 11-5974/O4
https://doi.org/10.26599/NR.2026.94909219

Review Article

Electrocatalytic upcycling of PET-derived ethylene glycol: Mechanism-guided catalyst design for selective glycolate and formate production

Qinyu Qu[1], Xueqi Wang[3], Chunxin Liu[4], Yumei Feng[1], Gengxu Han[3], Ruibo Wang[3], Zhijiong Wu[3], Ruisheng Yong[5], Zehui Yang[2](✉), Xiaoyang Fu[1](✉)

[1] State Key Laboratory of Advanced Waterproof Materials, School of Materials Science and Engineering, Peking University, Beijing 100871, China

[2] College of Materials and Chemical Engineering, China Three Gorges University, Yichang 443002, China

[3] CNPC Research Institute of Safety & Environment Technology, Dalian Department, Dalian 116031, China

[4] Beijing Grand Canal Energy Company Limited, Jinzhou Petrochemical Branch, Jinzhou 121001, China

[5] CNPC Research Institute of Safety & Environment Technology, Beijing 102206, China

Nano Res., **Just Accepted Manuscript** • https://doi.org/10.26599/NR.2026.94909219

https://www.sciopen.com/journal/1998-0124 on Sep. 24, 2026

© The Authors(s)

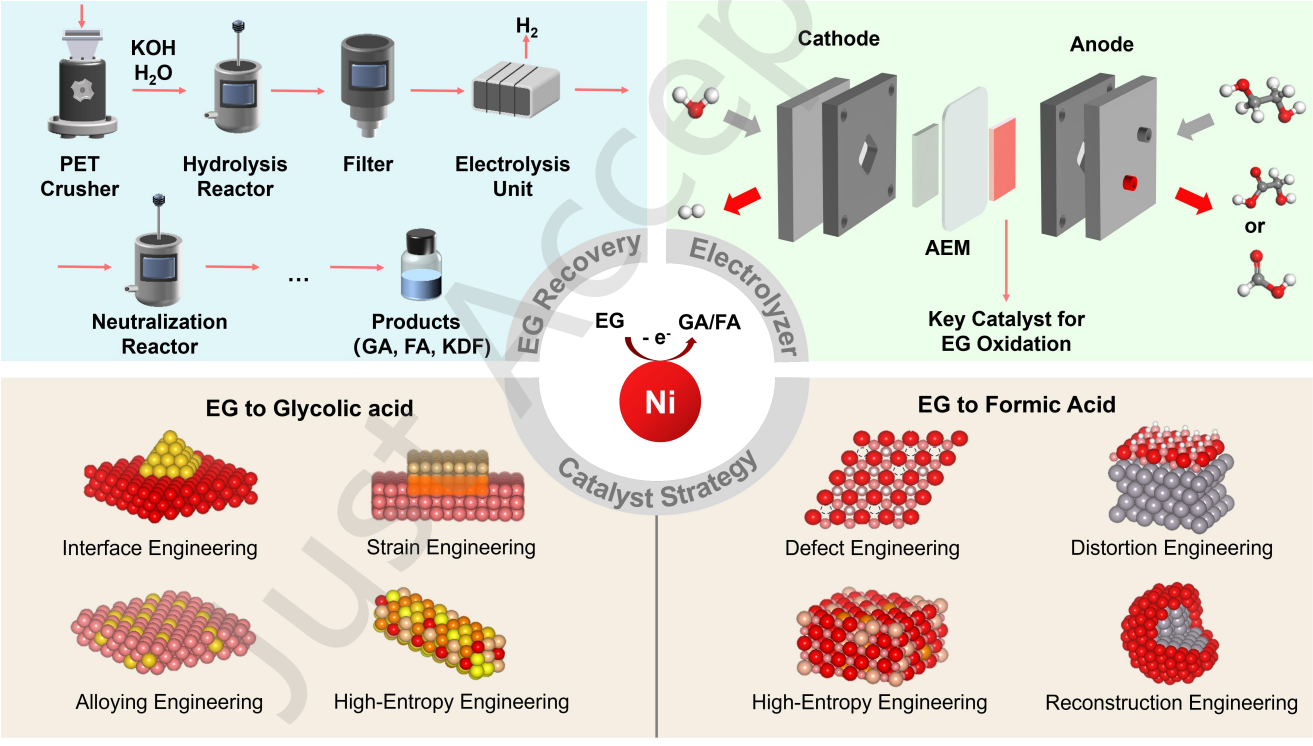
Just Accepted

This is a “Just Accepted” manuscript, which has been examined by the peer-review process and has been accepted for publication. A “Just Accepted” manuscript is published online shortly after its acceptance,which is prior to technical editing and formatting and author proofing. Tsinghua University Press (TUP) provides “Just Accepted” as an optional and free service which allows authors to make their results available to the research community as soon as possible after acceptance. After a manuscript has been technically edited and formatted, and the page proofs have been corrected, it will be removed from the “Just Accepted” web site and published officially with volume and article number (e.g., *Nano Research*, **2025**, *18*, 94906990). Please note that technical editing may introduce minor changes to the manuscript text and/or graphics which may affect the content, and all legal disclaimers that apply to the journal pertain. In no event shall TUP be held responsible for errors or consequences arising from the use of any information contained in these “Just Accepted” manuscripts. To cite this anuscript please use its Digital Object Identifier (DOI®),which is identical for all formats of publication.

Just Accepted

Electrocatalytic upcycling of PET-derived ethylene glycol: Mechanism-guided catalyst design for selective glycolate and formate production

TABLE OF CONTENTS (TOC)



Just Accepted

Electrocatalytic oxidation provides a direct route to valorize PET-derived ethylene glycol while co-producing hydrogen. This review connects glycolate/formate selectivity with reaction mechanisms and summarizes catalyst-design strategies for pathway regulation.

Nano Research | Review Article | Open Access

Electrocatalytic upcycling of PET-derived ethylene glycol: Mechanism-guided catalyst design for selective glycolate and formate production

Qinyu Qu[1], Xueqi Wang[3], Chunxin Liu[4], Yumei Feng[1], Gengxu Han[3], Ruibo Wang[3], Zhijiong Wu[3], Ruisheng Yong[5], Zehui Yang[2] ✉, Xiaoyang Fu[1] ✉

1 State Key Laboratory of Advanced Waterproof Materials, School of Materials Science and Engineering, Peking University, Beijing 100871, China

2 College of Materials and Chemical Engineering, China Three Gorges University, Yichang 443002, China

3 CNPC Research Institute of Safety & Environment Technology, Dalian Department, Dalian 116031, China

4 Beijing Grand Canal Energy Company Limited, Jinzhou Petrochemical Branch, Jinzhou 121001, China

5 CNPC Research Institute of Safety & Environment Technology, Beijing 102206, China

Received: 7 August 2026; **Revised:** 11 September 2026; **Accepted:** 24 September 2026

✉ Address correspondence to Zehui Yang, yeungzehui@gmail.com; Xiaoyang Fu, fuxy@pku.edu.cn

Cite this article: *Nano Research*, 2026, 19, 94909219 https://doi.org/10.26599/NR.2026.94909219

ABSTRACT: Polyethylene terephthalate (PET) is one of the most abundant polyester wastes, and its efficient upcycling remains a major challenge for circular materials management. Chemical upcycling, particularly alkaline hydrolysis, converts PET into terephthalate and ethylene glycol (EG), however, the water-soluble feature of EG complicates its separation from PET hydrolysates. Direct electrooxidation of PET-derived EG therefore provides an attractive route for coupling plastic valorization with cathodic hydrogen evolution. EG oxidation can proceed through C2-preserving pathways toward glycolate or through C-C-cleavage pathways to formate, which could be substantially converted to value-added glycolic acid or potassium diformate. Achieving selective conversion requires simultaneous control of hydroxyl activation, adsorption of oxygenated C2 intermediates, C-C bond retention or cleavage, and catalyst reconstruction under anodic conditions. This review summarizes recent advances in electrocatalytic upcycling of PET-derived EG, with emphasis on the mechanistic origins of glycolate and formate selectivity. Then, we introduce the electrocatalyst engineering strategies as guided by the mechanisms, including interfacial, alloying, strain, reconstruction, defect, and multicomponent (high entropy) engineering strategies in addition to their roles in regulating surface electronic structure, *OH adsorption and intermediates conversion. Finally, we outline opportunities for non-noble-metal catalysts for C2 pathway, dynamic potential pulse control, advanced in-situ characterizations and data-driven discovery of electrocatalysts.

KEYWORDS: polyethylene terephthalate upcycling; ethylene glycol electrooxidation; electrocatalyst design; reaction pathway regulation.

Just Accepted

1 Background

Nowadays, plastics are indispensable in modern society because of their low cost, light weight, durability, and diverse applications[1]. However, these characteristics also result in the difficulty in spontaneous degradation[2]. According to this situation, between 2020 and 2100, a cumulative total of approximately 10 billion tons of plastic will be generated[3]. As estimated, by 2050 approximately 12,000 million tons of plastic waste will accumulate in landfills or the natural environment[4].

Polyethylene terephthalate (PET) is a representative polyester with an annual production of approximately 70 million tons. It is commonly used in packaging, textiles, electronic insulation coatings, and battery composite copper foils[5]. However, only a limited fraction of waste PET is effectively recycled, while much of the remaining waste is landfilled, incinerated, or released into the environment[6-8]. Conventionally, PET recycling methods (Fig. 1) include energy recovery (e. g., incineration) and material recovery (e. g. physical recycling, biological recycling, and chemical recycling)[9]. Incineration can only recover a portion of the

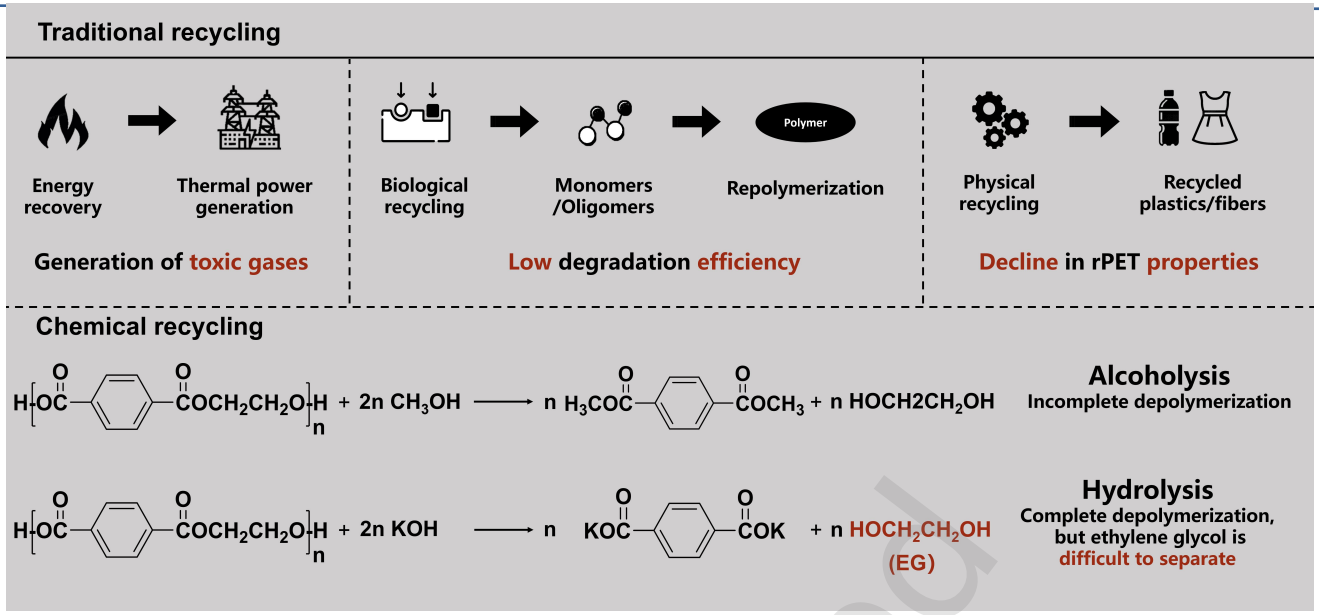


Figure 1 The traditional PET recycling strategies.

energy while generating hazardous gases and carbon emissions. Physical recycling leads to the cleavage of polymer chains, resulting in degraded mechanical properties of the recycled materials and downgraded commercial applications[10]. Therefore, developing effective methods for PET recovery and upcycling represents a novel and vital direction for sustainable plastics management[10-15]

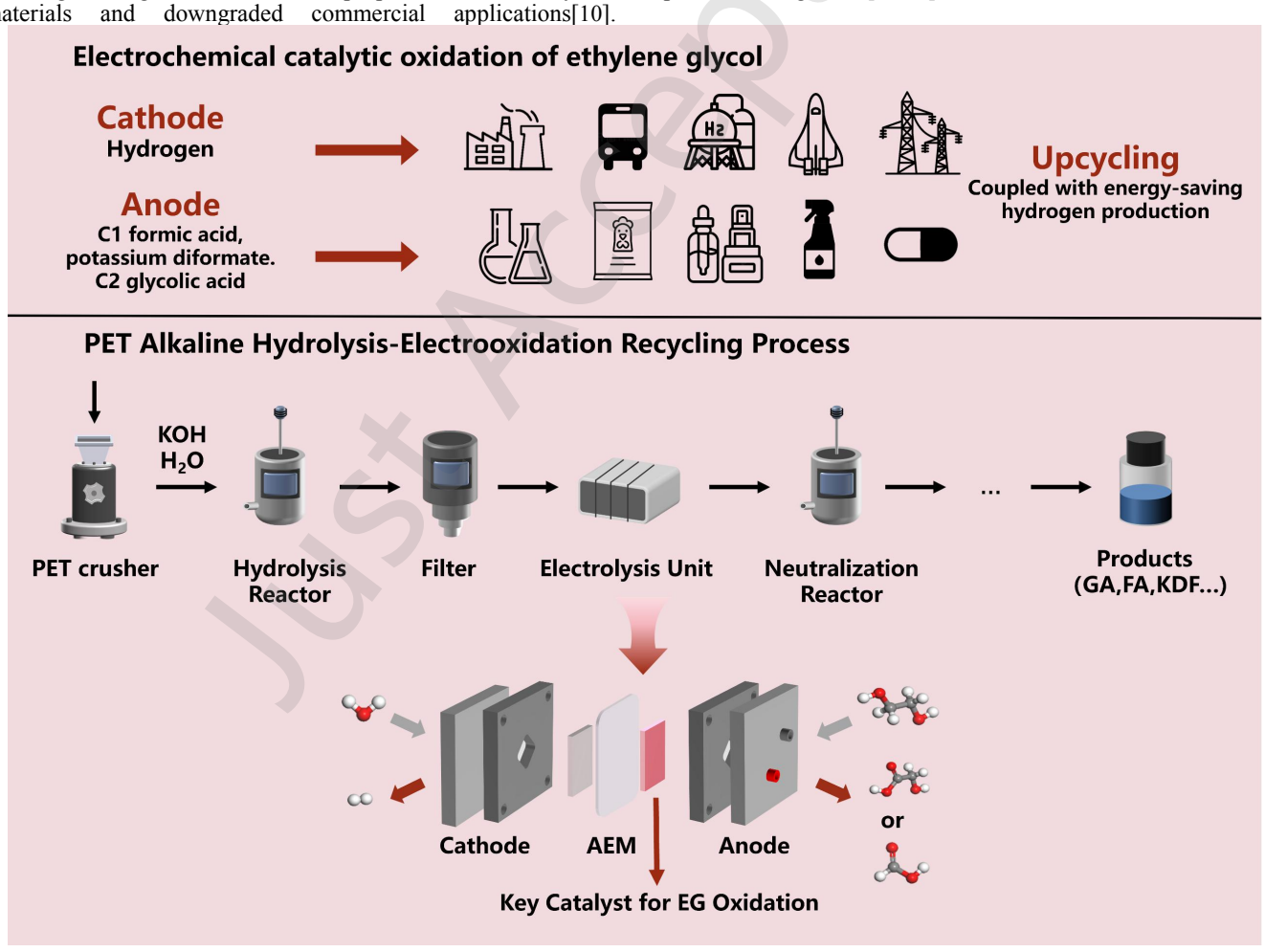


Figure 2 PET Upcycling via Electrocatalytic Oxidation of Ethylene Glycol.

Chemical recycling via depolymerization enables the recovery of PET-derived molecular building blocks through hydrolysis[16], methanolysis[17, 18], ammonolysis[19], hydrosilylation[20], and hydrogenolysis[21], although sustainable conversion into value-added chemicals remains challenging[22, 23]. Methanolysis produces dimethyl terephthalate and EG but may suffer from incomplete conversion because of thermodynamic limitations[24]. In

Just Accepted

contrast, alkaline hydrolysis efficiently yields terephthalate salts and EG[25], the former can be recovered as TPA by acidification and precipitation, whereas EG is difficult to separate because of its water solubility and high boiling point[26]. Consequently, low-cost upgrading strategies[27], particularly electrochemical reforming under alkaline conditions[28-32], provide an attractive route for directly converting PET-derived EG into readily separable and value-added products. As shown in Fig. 2, PET is first crushed and hydrolyzed under alkaline conditions. The hydrolysate consists of potassium terephthalate and ethylene glycol and after filtration, the hydrolysate will be directly fed into an electrolyzer, the EG from the PET hydrolysate can undergo EG oxidation reaction (EGOR) into glycolate and formate products, which could be substantially acidified and separated as value-added glycolic acid (GA), formic acid (FA) and potassium diformate (KDF), etc, while the terephthalate is electrochemically stable in general. Importantly, the C2 pathway product, GA, is an α-hydroxy acid extensively applied in skincare products and precursor for biodegradable plastics, PGA. Regarding the C1 pathway product, formic acid has high volumetric hydrogen capacity (53 g H_2/L), low toxicity, and limited flammability at ambient temperature, making it a promising liquid hydrogen carrier[33]. Its derivative, KDF, serves predominantly as an antibiotic-free feed additive that can improve growth performance of farm animals by lowering gastrointestinal pH and suppressing pathogenic bacteria[34]. Additionally, on the cathode side, hydrogen evolution reaction (HER) will concurrently occur, contributing to energy-efficient hydrogen production because of the lower anodic potential for EGOR compared with oxygen evolution reaction. The electrolysis unit shown in Fig. 2 illustrates a typical membrane electrode assembly (MEA) for EGOR[23, 27, 28, 35, 36]. It consists of anion exchange membrane (AEM), gas-diffusion layers and catalyst layers from both anodes and cathodes. During operation, the alkaline electrolyte containing EG is circulated and supplied to the anode, where EG is oxidized into value-added products. Electrons flow through the external circuit to drive the cathodic HER, while the hydroxide anion transport through the AEM maintains charge balance.

2 EGOR Pathways and Electrocatalyst Design

At the anode, EGOR proceeds mainly through the C2 pathway toward glycolic acid (GA) and the C1 pathway toward formic acid (FA)[37]. Coupled with cathodic hydrogen evolution, PET-derived EG electro-reforming can operate under mild conditions using renewable electricity to co-produce value-added chemicals and hydrogen[38-43]. Therefore, understanding catalyst evolution and reaction mechanisms is essential for designing active and selective EGOR anodes[44, 45].

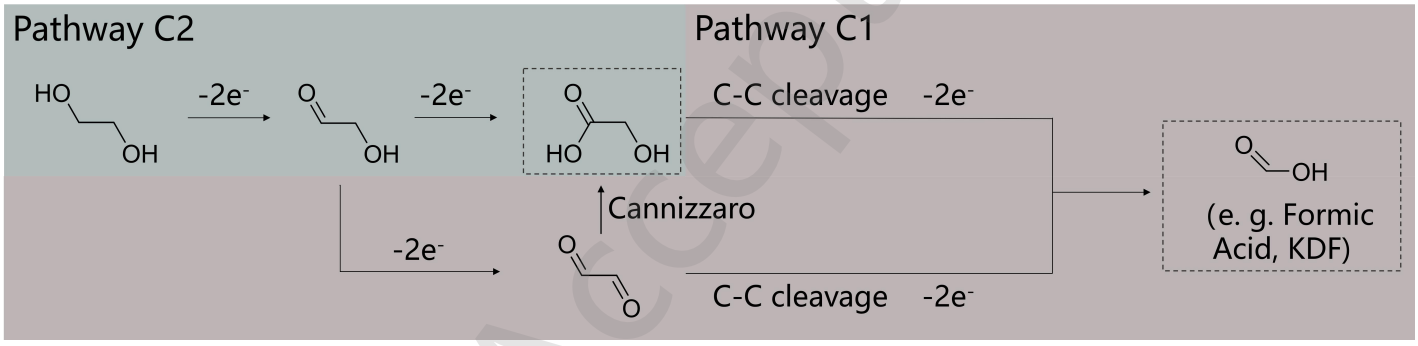


Figure 3 Ethylene Glycol Electrooxidation Pathways (Pathway C1 and Pathway C2).

In the C2 pathway for valuable GA production, EG first undergoes 2e- oxidation to glycolaldehyde (*$CHOCH_2OH$), followed by another 2e- oxidation to GA (*$HOOCCH_2OH$) with *$OCCH_2OH$ as the key intermediate. Glyoxal (*CHOCHO) is an alternative product from 4e- oxidation, which tends undergo a Cannizzaro reaction[46] to GA. In the C1 pathway for FA production, both *CHOCHO and *$COOHCH_2OH$ can undergo non-Faradaic C-C cleavage, leading to *CHO intermediates[47], *COOH and *CH_2OH intermediates, respectively. Subsequently, another 2e- transfer will takes place, leading to 2 equimolar FA as the final product, with an overall 6e- transfer[46].

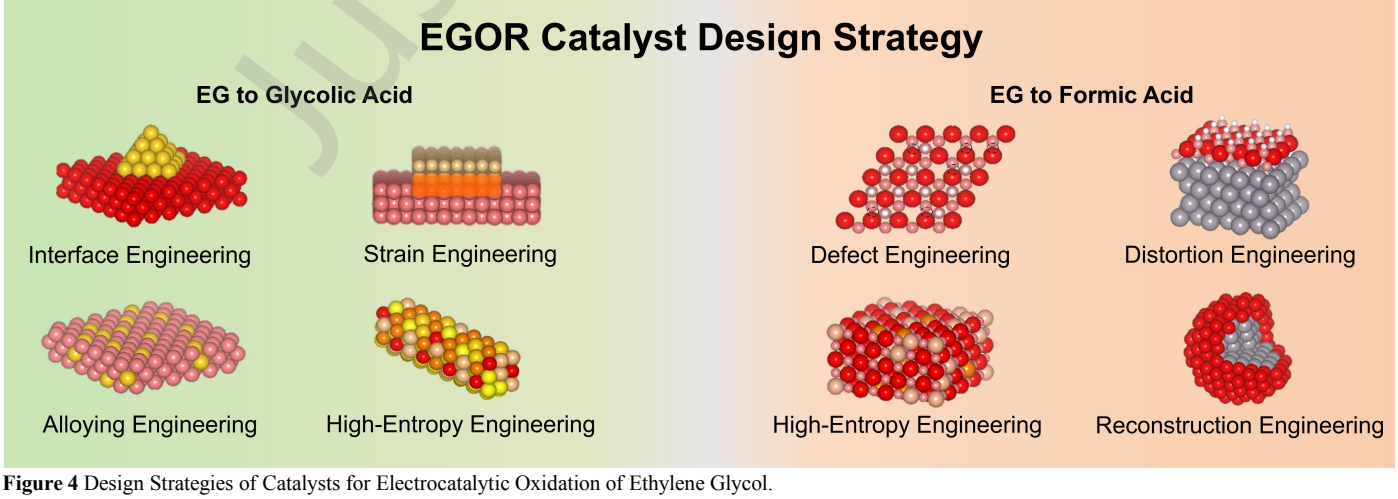


Figure 4 Design Strategies of Catalysts for Electrocatalytic Oxidation of Ethylene Glycol.

EGOR involves multiple deprotonations, electron-transfer, hydroxyl-adsorption, and intermediate-conversion steps, resulting in complex reaction networks and sluggish kinetics in the absence of efficient catalysts. The initial conversion of EG to

Just Accepted

*$CHOCH_2OH$ could proceed through different adsorption configurations, such as *$CHOHCH_2OH$ and *OCH_2CH_2OH transition states and the free energy barrier depends strongly on the catalyst surface[48]. In addition, the hydroxyl availability and neighboring-site interactions can directly influence the thermodynamics and kinetics of subsequent oxidation and C-C bond cleavage or retention[48, 49]. Therefore, an efficient EGOR catalyst should not merely lower the overall reaction barrier, but should establish a balanced free energy diagram for EG adsorption, hydroxyl activation, intermediate conversion, controlled C-C bond retention or cleavage and product desorption.

Previous studies have shown that *OH plays two major roles in determining the activity and product selectivity of EGOR. First, *OH can promote O-H/C-H bond activation and the subsequent oxidation of carbonyl-containing intermediates. Specifically, *OH can participate in proton-electron transfer processes or provide reactive surface oxygen species, thereby facilitating the further oxidation of the C2 intermediate *COCH2OH into *HOOCCH2OH[28, 50, 51].Second, *OH can facilitate the oxidation and removal of carbonyl-containing intermediates. If these intermediates remain strongly adsorbed on Pt/Pd surfaces for prolonged periods, they may occupy active sites and cause surface poisoning. The introduction of *OH promotes the oxidation of these strongly adsorbed carbonyl-containing species and weakens their persistent adsorption on the catalyst surface, thereby releasing active sites for subsequent catalytic turnover[52]. For the C2 pathway, an adequate supply of *OH, relatively weak glycolate adsorption, and a sufficiently high barrier for C-C bond cleavage act synergistically to enable the rapid conversion of carbonyl-containing intermediates and the timely desorption of products from the catalyst surface, thereby favoring glycolate formation.

For the C1 pathway, sufficient *OH can promote more extensive oxidation, whereas C-C bond cleavage is more directly governed by the intrinsic ability of the catalyst to lower the C-C cleavage barrier[53],The synergistic effect of these two factors promotes selectivity toward C1 products.

Therefore, achieving high selectivity in EGOR results from a delicate balance among multiple factors, including the amount and surface coverage of *OH, intermediate adsorption strength, the C-C bond cleavage barrier, and product adsorption.

This review categorizes the catalysts into two main types based on their reaction pathways (Fig. 4). The catalyst design strategies for C2 pathway (EG to GA) are summarized as interface, alloy, strain, and high-entropy engineerings[25, 27, 28, 48, 51, 54-60]. The catalyst design strategies for C1 pathway (EG to FA) are concluded as distortion, reconstruction, defect, and high-entropy engineerings[14, 23, 46, 61-69].

The essence of different catalyst-design strategies is not that each strategy simply corresponds to a particular material structure. Rather, these strategies regulate the competition between selective oxidation and C-C bond cleavage by altering the adsorption energies of key intermediates and *OH as well as the associated reaction energy barriers. When C2 intermediates can be rapidly oxidized and desorbed while C-C bond cleavage is suppressed, the reaction preferentially produces glycolate. In contrast, when the catalyst surface more effectively stabilizes high-valent oxygen species and the transition states associated with C-C bond cleavage, further oxidation becomes more favorable, resulting in the formation of formate.

Table 1. Representative electrocatalysts for selective EG oxidation to glycolate/glycolic acid (GA).

Catalyst	Electrolyte	Electrochemical activity	Product FE / selectivity	Stability	Cell / operation mode	Ref.
Pt/γ-NiOOH/NF	1.0 M KOH + 0.30 M EG	E@150 = 0.60 V; $j_{max} \approx 450$ mA cm^{-2}	FE_{GA} >90%; S_{GA} >90%	10 h @ 0.55 V	Three-electrode (model EG)	[27]
Pt/γ-NiOOH/NF	Real PET hydrolysate (alkaline)	V_{cell}@130 = 0.80 V	FE_{GA} >90%; S_{GA} >90%	10 h closed-loop electrolysis	MEA flow cell (real PET hydrolysate; EGOR || HER)	[27]
PdAg/NF	0.50 M KOH + 1.0 M EG	E@10 = 0.57 V; j ≈ 300 mA cm^{-2} before dominant OER	FE_{GA} = 92% @ 0.91 V	2 h CA; long-term durability NR	Three-electrode (paired HER also demonstrated)	[55]
Pd-$Ni(OH)_2$/NF	1.0 M KOH + 1.0 M EG	E@600 = 1.15 V	FE_{GA} >85% (0.7-1.2 V); $S_{GA,max}$ = 91.6%	>200 h	Three-electrode; flow-electrolyzer durability test	[51]
Pd/$NiMoO_4$/NF	1.0 M NaOH + 1.0 M EG	j_{max} = 1.2 A cm-2 (9 M NaOH + 1 M EG)	FE_{GA} = 95.7% @ 1.0 V; 93.1-99.9% during durability test	1500 h intermittent electrolysis; no significant FE/charge loss	Three-electrode (cyclic electrolysis)	[56]
Pt_1/RuO_2	1.0 M KOH + 0.50 M EG	Mass activity = 8.09 A $mgPt^{-1}$	FE_{GA} = 95.3%; S_{GA} = 96.9% @ 0.80 V	20 consecutive cycles; FE/selectivity retained	Three-electrode	[54]
Pt_1/RuO_2	Anolyte: 3.0 M KOH + 1.0 M EG; catholyte: 3.0 M KOH; 50 °C	I = 6 A (100 cm^2 MEA)	GA production demonstrated; MEA FE/selectivity NR	>500 h @ 6 A	100 cm^2 two-electrode MEA flow cell	[54]
PdCu/$Ni(OH)_2$	Alkaline EG electrolyte (concentration NR in abstract)	E@2000 = 1.22 V	FE_{GA} = 97.7% @ 500 mA cm^{-2}	NR	High-current EGOR (PV-driven HER || EGOR demonstrated)	[36]

Just Accepted

Catalyst	Electrolyte	Electrochemical activity	Product FE / selectivity	Stability	Cell / operation mode	Ref.
PtPd-Ni(OH)$_2$	Alkaline EG electrolyte (concentration NR in abstract)	E@≈200 = 0.69 V	FE_{GA} = 90.38%	>700 h	Long-duration electrolysis	[70]
Pd/NF-1	1.0 M KOH + 0.30 M EG	EPC = 0.33-1.23 V; j_{peak} >100 mA cm^{-2}	FE_{GA} = 97.84% (EPC); 96.45% (constant potential)	60 h under EPC; minimal deactivation	Electrochemical potential cycling (flow-cell validation)	[59]
Ir_1Pd single-atom alloy	Neutral electrolyte (EG concentration NR in abstract)	j_{peak} = 56.2 mA cm^{-2} @ 0.89 V	FE_{GA} = 76.3%; S_{GA} = 80.1%	>330 h	Three-electrode (neutral medium)	[50]
Pt@Ni(OH)$_{2-x}$	Alkaline EGOR (concentrations NR in abstract)	E@355.1 = 0.90 V (C2-selective regime)	S_{GA} = 95%	NR	Potential-controlled C2/C1 switching (real-PET flow reactor)	[71]

Notes: E@j denotes the anodic potential (V vs. RHE) required to reach a geometric current density j (mA cm^{-2}). V_{cell}@j denotes the full-cell voltage at j. j_{max} and j_{peak} denote maximum and peak current density, respectively. FE_{GA}/$FE_{formate}$ and S_{GA}/$S_{formate}$ denote Faradaic efficiency and selectivity for glycolate/formate. CA = chronoamperometry; EPC = electrochemical potential cycling; NR = not reported or not unambiguously extractable; N/A = not applicable. Full-cell/MEA voltages should not be directly compared with three-electrode potentials vs. RHE.

*For Pd/NiMoO$_4$/NF, E@100 was measured in 1.0 M NaOH + 1.0 M EG, whereas the reported 1.2 A cm^{-2} high-current value was obtained in 9 M NaOH + 1 M EG. MEA total current (A) and full-cell voltage (V_{cell}) should not be directly compared with geometric current density and half-cell potential, respectively.

Table 2. Representative electrocatalysts for selective EG oxidation to formate/formic acid (FA).

Catalyst	Electrolyte	Electrochemical activity	Product FE / selectivity	Stability	Cell / operation mode	Ref.
$NiSe_2$	1.0 M KOH + 1.0 M EG	E@50 = 1.395 V; j ≈ 95 mA cm^{-2} @ 1.60 V	$FE_{formate}$ >80%	10 h @ 1.60 V; 48 h extended test reported	Three-electrode	[63]
$NiCu_{60s}$/NF	1.0 M KOH + 0.30 M EG	ΔE100(EGOR-OER) = -0.307 V; FE benchmark @ 1.47 V	$FE_{formate}$ = 95.8% @ 1.47 V; >80% with commercial PET hydrolysate	24 h; similar surface states after 2 and 24 h	Three-electrode H-cell (real PET hydrolysate also tested)	[64]
Co,Cl-NiS/NF	1.0 M KOH + 0.10 M EG	j >300 mA cm^{-2} evaluated; FE benchmark @ 1.50 V	$FE_{formate}$ = 93.5%; $S_{formate}$ = 93.9% @ 1.50 V	12 h CA; ~86% activity retained	Three-electrode	[72]
Co,Cl-NiS/NF	Anolyte: 2.0 M KOH + 20 g L^{-1} PET hydrolysate; catholyte: 2.0 M KOH	V_{cell}@10/100/200 = 1.17/1.51/1.55 V	Formate confirmed; MEA FE/selectivity NR	24 h PET-hydrolysate electrolysis	MEA flow cell	[72]
$Pt_1/Ni(OH)_2$-3	1.0 M KOH + 0.10 M EG	E@≈1000 = 1.444 V	$FE_{formate}$ >90%; $S_{formate}$ >90%	5 consecutive CA runs; no noticeable loss in yield/FE	Three-electrode H-cell	[35]
$Pt_1/Ni(OH)_2$-3	Real PET hydrolysate (alkaline)	Ampere-level operation; V_{cell} NR	Formate yield = 98.4%; $FE_{formate}$ = 88.3% (initial MEA test)	500 h continuous ampere-level operation; high FE maintained	Zero-gap MEA (real PET hydrolysate)	[35]
NiFe-sc-PBA/NF	3.0 M KOH + 1.0 M EG (activity); 3.0 M KOH + 0.30 M EG (FE)	E@500 = 1.484 V; E@1000 = 1.625 V	$FE_{formate,max}$ ≈ 98.5%; >90% during stability test @ 1.60 V	>50 h @ 1.60 V; FE >90%	Three-electrode H-cell	[69]

Just Accepted

Catalyst	Electrolyte	Electrochemical activity	Product FE / selectivity	Stability	Cell / operation mode	Ref.
NiFe-sc-PBA/NF	Anolyte: 1.0 M KOH + 1.0 M EG; catholyte: 1.0 M KOH	V_{cell}@1000 = 1.88 V; V_{cell}@2000 = 2.03 V (50 °C)	$FE_{formate}$ >90% (0.2-1.8 A cm^{-2}); >92% @ 1.5 A cm^{-2}	>500 h @ stepwise 1.0/1.5 A cm^{-2}; no performance degradation	MEA flow cell	[69]
$Ni(OH)_2$/NF	10 M KOH + 0.30 M EG	j >500 mA cm^{-2} @ 1.60 V	$FE_{formate}$ = 93.2%; $S_{formate}$ ≈96%	~40 h / 10 PET-hydrolysate cycles; ~500 mA cm^{-2} maintained	Three-electrode (repeated PET-hydrolysate electrolysis)	[73]
Pt@$Ni(OH)_{2-x}$	Alkaline EGOR (concentrations NR in abstract)	E@382.3 = 1.60 V (C1-selective regime)	$S_{formate}$ = 92%	NR	Potential-controlled C2/C1 switching (real-PET flow reactor)	[71]

Notes: E@j denotes the anodic potential (V vs. RHE) required to reach a geometric current density j (mA cm^{-2}). V_{cell}@j denotes the full-cell voltage at j. j_{max} and j_{peak} denote maximum and peak current density, respectively. FEGA/FEformate and $S_{GA}/S_{formate}$ denote Faradaic efficiency and selectivity for glycolate/formate. CA = chronoamperometry; EPC = electrochemical potential cycling; NR = not reported or not unambiguously extractable; N/A = not applicable. Full-cell/MEA voltages should not be directly compared with three-electrode potentials vs. RHE.

3 Electrooxidation of Ethylene Glycol to Glycolic Acid

The oxidation of EG to GA proceeds through a C-C bond-preserving pathway, in which one terminal hydroxymethyl group undergoes a four-electron oxidation while the carbon backbone remains intact. This process generally involves stepwise dehydrogenation and oxygenation through glycolaldehyde- and/or glyoxal-related intermediates, ultimately yielding GA[28, 51]. Therefore, selectively oxidizing one hydroxymethyl group while suppressing C-C bond cleavage remains the major challenge[28].

Ni-based catalysts typically require relatively high potential to generate the active NiOOH phase for EGOR. However, the strong oxidizing nature of NiOOH can promote C-C bond cleavage, leading predominantly to formate products and thus disfavoring the C2 pathway[74]. Incorporating noble-metal sites is therefore an effective strategy for promoting the C2 pathway. Pt- and Pd-based electrodes exhibit high intrinsic EGOR activity, with apparent glycolate Faradaic efficiency exceeding 85% in alkaline media[75]. Nevertheless, their practical application is limited by high cost and the poisoning of active sites by strongly adsorbed carbonyl intermediates[76]. Therefore, developing noble-metal-based electrocatalysts with high activity, selectivity, durability, and reduced noble-metal loading remains a central objective in this field.

Mechanism of the C2 pathway involves the adsorption of EG, dehydrogenation, intermediates conversion, and the GA desorption. Additionally, the participation of *OH is also required during the oxidative conversion[51]. An ideal electrocatalyst should have balanced free-energy profile for the EG adsorption, *OH generation, intermediate conversion and GA desorption, while avoiding excessive C-C bond cleavage and surface poisoning. Noble-metal-based electrocatalysts, particularly Pd- and Pt-containing systems, generally favor the C2-preserving oxidation pathway because they can efficiently activate the O-H and C-H bonds of EG while maintaining a comparatively unfavorable kinetic environment for direct C-C bond cleavage. At appropriate anodic potentials, this balance promotes stepwise dehydrogenation and oxidation of EG-derived C2 intermediates toward glycolate while preserving the carbon backbone[77, 78].Thus, noble-metal-based catalysts tend to favor C2-preserving EG oxidation within an appropriate potential window[79], whereas increasing anodic polarization can shift the surface chemistry toward deeper oxidation and C-C cleavage, thereby decreasing C2 selectivity.

Achieving such regulations requires the collaborative optimization of local electronic structure, coordination environment, *OH species supply and intermediate-binding strength. To this end, interfacial, alloying, strain, and high-entropy engineerings have emerged as four strategies. Interfacial engineering spatially separates and couples EG activation sites and *OH adsorption sites; alloying engineering tunes the electronic structure and adsorption behavior of noble-metal centers; strain engineering modulates electronic structure and surface reactivity through lattice distortion; and high-entropy engineering creates diverse local atomic ensembles and energy profiles to favor EG adsorption and conversion. The following sections discuss how these strategies regulate key reaction steps and promote selective GA formation from EG.

3.1 Interface Engineering

Interfacial engineering provides an effective strategy for constructing spatially separated yet synergistic active sites by regulating local coordination, electronic structure, and intermediate-binding strength at heterointerfaces[80, 81]. For C2-selective EGOR, noble metals such as Pd and Pt, which favor EG activation and C-C bond retention[54, 55, 82, 83] are commonly coupled with oxophilic Ni-based supports, such as oxides, hydroxides or oxyhydroxides. This bifunctional configuration enables a division of labor in which noble-metal sites activate EG, while the oxophilic component promotes OH^- adsorption and *OH generation, facilitates intermediate oxidation, and suppresses the accumulation of strongly adsorbed carbonyl intermediates. Consequently, such interfaces can lower reaction barriers and improve GA selectivity and catalyst stability.

Under Review

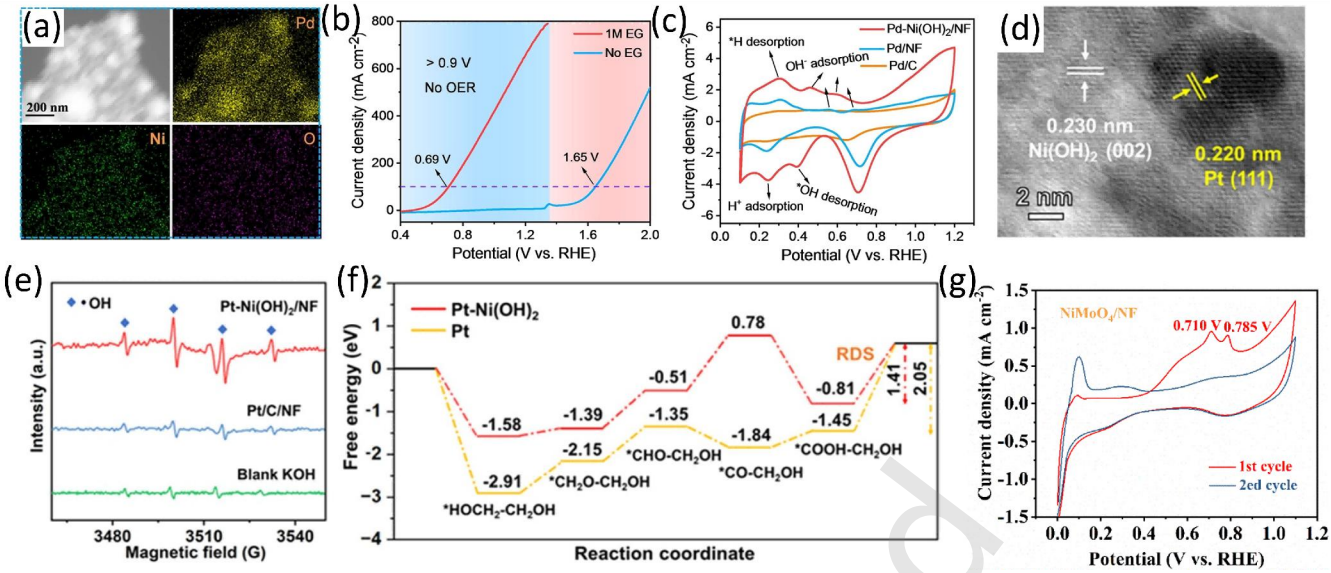


Figure 5 (a) The corresponding elemental mapping images of Pd-Ni(OH)$_2$. (b) LSV curves for Pd-Ni(OH)$_2$/NF in 1.0 M KOH with and without EG. (c) CV curves of Pd-Ni(OH)$_2$/NF, Pd/NF and Pd/C in 1 M KOH. (d) HRTEM images of Pt-Ni(OH)$_2$/NF. (e) EPR detection of DMPO-•OH of EGOR on Pt-Ni(OH)$_2$ and Pt. (f) Free-energy diagram.(g) CO stripping experiments of NiMoO$_4$/NF. (a)-(c) Reproduced with permission.[51] Copyright 2023 *Wiley-VCH GmbH.* (d)-(f) Reproduced with permission. [28] Copyright 2023 *American Chemical Society.* (g) Reproduced with permission. [56] Copyright 2024*The Author(s).*

Compared to Pt, Pd electrodes exhibit relatively low activity for in cleaving C-C bonds due to its inferior deprotonation efficiency[82]. For this reason, Pd is often chosen to construct highly selective EGOR catalysts. Liu et al.[51] successfully synthesized Pd-Ni(OH)$_2$/NF catalyst through the synergistic interaction between Pd and Ni(OH)$_2$. Elemental mappings (Fig. 5a) show the uniform distribution of Pd, Ni, and O in the nanosheets, verifying the formation of Pd-Ni(OH)$_2$ nanohybrids. Compared with the other control groups, upon the addition of 0.1 M EG, Pd-Ni(OH)$_2$/NF exhibited a more pronounced decrease in the open-circuit potential (OCP) (Δ = 0.50 V), greater than that observed for Pd/NF (Δ = 0.44 V) and Pd/C (Δ = 0.11 V), indicating that EG adsorption is more favorable on Pd-Ni(OH)$_2$/NF. Pd-Ni(OH)$_2$/NF displays efficient electrooxidation of EG to GA with a high Faraday efficiency (FE) (>85%) and selectivity (>90%) even at an industry-level current density (600 mA cm^{-2} at 1.15 V vs. RHE). In comparison, the selectivity of Pd/NF, Pd/C, and Pd2Ni alloy were 73.9%, 79.1%, and 83.5%, respectively. Crystal plane analysis reveals that cubic Pd exposes (111) and (200) planes, while Ni(OH)$_2$ exposes (002) facet. LSV results (Fig. 5b) indicates the catalyst delivers 100 mA cm^{-2} at 0.69 V vs. RHE, which is 910 mV lower than the potential required in the OER catalysis. A weak oxidation peak corresponding to Ni^{2+}/Ni^{3+} was also observed at the OER potential (1.39 V vs. RHE), implying surface restructuring process. DFT calculations confirm that EG adsorption occurs preferentially at the Pd sites. The adsorption energy of EG on Pd-Ni(OH)$_2$ (-1.12 eV) was stronger than on pure Pd (-0.94 eV), identifying Pd as the main active center for EG adsorption. Moreover, the introduction of Ni(OH)$_2$ optimizes the adsorption behavior of Pd through electronic modulation. Pd-Ni(OH)$_2$/NF exhibits outstanding stability, with negligible current decay after 200 hours of continuous operation. Comprehensive post-stability characterizations further confirm the well-preserved structure and composition, supporting the high stability of the catalyst[51]. From the perspective of bifunctional synergy, the oxophilic nature of Ni(OH)$_2$ (Fig. 5c) enables the adsorption of OH^- to *OH at a low potential of 0.4 V vs. RHE, which further assists the conversion of *OCCH$_2$OH intermediate to GA. Furthermore, charge density difference and Bader charge analysis verify the strong electronic interaction at the Pd-Ni(OH)$_2$ interface with 1.71 electrons transferred from Pd to Ni(OH)$_2$, which reduces the electron density of Pd and downshifts its d-band center to -1.87 eV. This weakens the interaction between Pd 3d orbitals and 2π orbitals from *CO intermediates, thereby decreasing the adsorption strength to prevent the active sites poisoning. Moving one step further, the authors extended this strategy to other oxophilic supports loaded with noble metals for EG-to-GA conversion[54], demonstrating the universality of the noble metal/oxophilic support design.

Liu et al.[28] adopted a similar strategy based on the synergistic interaction between Pt and Ni(OH)$_2$ to optimize the adsorption and desorption behaviors of *OH and intermediates on metal sites, thus achieving enhanced EGOR activity, selectivity, and stability. Crystal structure analysis (Fig. 5d) shows that cubic Pt exposes the (111) facet, while Ni(OH)$_2$ exposes the (002) facet. Affected by the electronic modulation from Ni(OH)$_2$, the d-band center of Pt is downshifted to -2.12 eV. This weakens the adsorption of *HOOCCH$_2$OH on Pt and facilitates the desorption as GA, rather than over oxidation into C1 products (e.g., FA). As shown in Fig. 5e, *OH accumulation is much higher on Pt-Ni(OH)$_2$/NF than on Pt/C/NF, indicating that active Pt sites are less poisoned by the intermediates[28]. DFT calculations (Fig. 5f) reveal that Pt-Ni(OH)$_2$ lowers the free energy barrier for GA desorption from 2.05 eV to 1.41 eV, accelerating the reaction rate and enabling 100 mA cm^{-2} at a low potential of 0.69 V vs. RHE.

For the catalyst Pd/NiMoO$_4$/NF developed by Kai Shi et al.[56], electrons transfer from Pd to NiMoO$_4$, generating positively charged Pd species. This promotes OH^- migration to the Pd surface and increases the local hydroxyl concentration. CO stripping voltammetry (Fig. 5g) shows that the CO oxidation peak potential of Pd/NiMoO$_4$/NF negatively shifts from 1.090 V (Pd/NF) to 1.026 V vs. RHE, indicating weakened CO adsorption on Pd and easier oxidative removal, thus enhancing EGOR stability. Pd/NiMoO$_4$/NF exhibited a Faradaic efficiency (FE) of up to 98.9% for glycolic acid, whereas Pd/NF showed an FE of only 87-88%. In addition, the GA yield of Pd/NiMoO$_4$/NF reached 98.8%, which was significantly higher than that of the comparison samples., a high Faradaic efficiency of 98.9%, a high yield of 98.8%, and outstanding stability (1500 h) for EG electrooxidation.

Similarly, in the catalyst Pt/γ-NiOOH/NF prepared by Mengmeng Du et al.[27], the low Pt loading (0.9 wt%, 0.18 mg cm^{-2}) reduces cost while maintaining high catalytic activity,

Not Accepted

demonstrating the high specific activity of noble-metal sites toward EGOR. γ-NiOOH also provides abundant *OH active species that participate in the initial dehydrogenation of EG and lower the reaction energy barrier. Obvious charge accumulation occurs at the Pt/γ-NiOOH interface, optimizing EG adsorption energy and reducing the energy barrier of the rate-determining step.

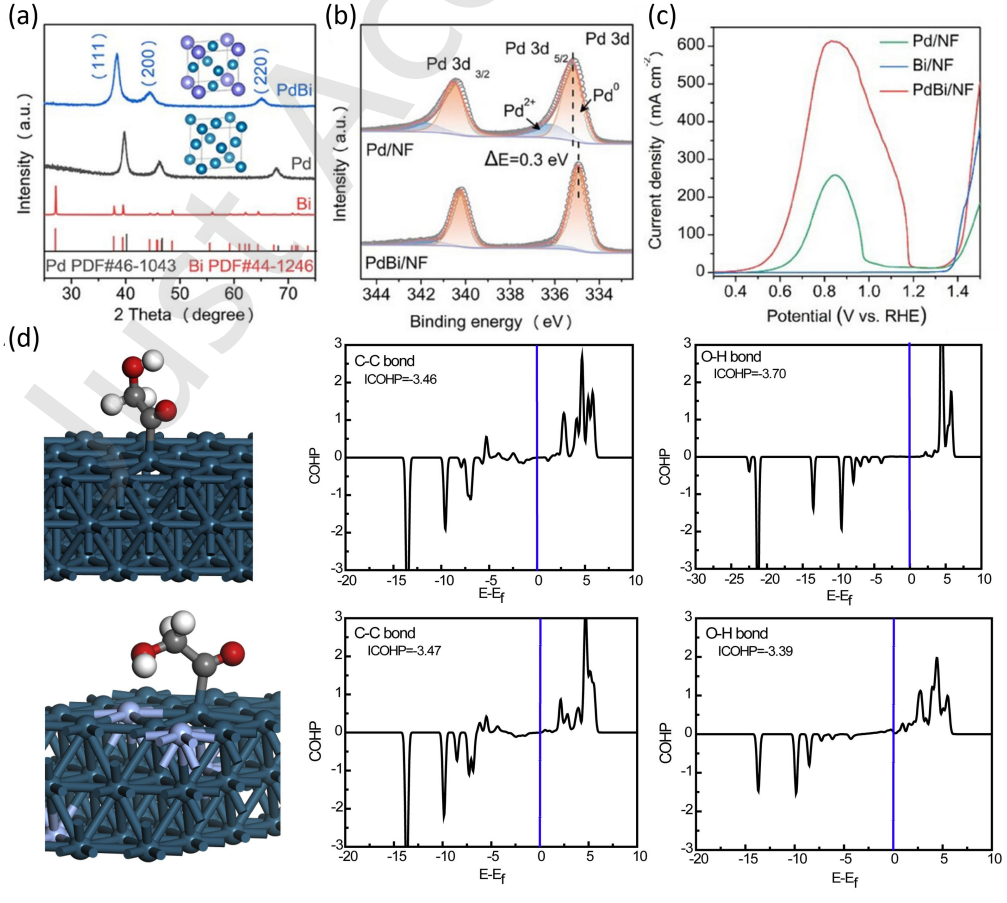
Additionally, Yan et al.[25] proposed that *OH groups on $Ni(OH)_2$ can form hydrogen bonds with the -OH groups from EG, thus enriching EG near the surface. Au tends to activate -OH in EG rather than break C-C bonds, thus improving GA selectivity. The Au/$Ni(OH)_2$ interface stabilizes key intermediates through σ bonds (Au-alkoxy) and hydrogen bonds between $Ni(OH)_2$ and hydroxyl from EG, suppressing the formation of C1 byproducts such as FA. This work reveals that $Ni(OH)_2$ not only indirectly regulates the adsorption of EG on noble metal sites via electronic effects but also directly promotes EG enrichment through hydrogen-bonding interactions, providing a new strategy to enhance EGOR activity and selectivity.

3.2 Alloying Engineering

Alloying is a traditional approach for tuning the composition and electronic properties of noble-metal catalysts. Introducing a second or third metal can alter the local coordination environment and electronic structure to modulate adsorption energy of reaction intermediates.[84-88].

Sailei Kang et al. [48] developed an alloy catalyst PdBi/NF. As shown in Fig. 6a, the X-ray diffraction (XRD) indicates the negatively shifted diffraction peaks of PdBi compared with monometallic Pd, confirming the formation of PdBi alloy phase, which is further confirmed from the energy-dispersive spectroscopy (EDS) mapping. Regarding the XPS spectrum in Fig. 6b, the peak at 334.9 eV corresponds to Pd^0 from PdBi/NF [89] with a negative shift of 0.3 eV compared with PdBi/NF, indicating that electrons transfer from Bi to Pd. The strong electronic interaction between Pd and Bi leads to the downshift of the d-band center of Pd, which weakens the adsorption of intermediates and promotes the timely desorption of GA to avoids further oxidation, leading to more than 2-fold enhanced EGOR performance (Fig. 6c), in addition to stability performance for 10 hour and robust Faradaic efficiency of 99% for GA production,in comparison, the GA selectivity of Pd/NF was 91%. Thanks to the concurrent improvement in activity and selectivity, the GA productivity of PdBi/NF reached 2.06 mmol cm^{-2} h^{-1}, which was approximately six times higher than that of Pd/NF (0.34 mmol cm^{-2} h^{-1}). DFT calculations show that EG is adsorbed on the PdBi surface through a bridge adsorption mode, compared with the monodentate adsorption mode (with *$CH_2OHCHOH$ as the intermediate), the bridge adsorption mode has a lower energy barrier, with *CH_2OHCH_2O as the intermediate.

The PdAg/NF catalyst developed by Di Si et al.[55] via the similar design rationale: electrons transfer from Ag to Pd, resulting in the downshift of the d-band center of Pd, which weakens the adsorption energy of intermediates and products, thus avoiding catalyst poisoning and over-oxidation. The Ag sites lose electrons and become positively charged, and the adsorbed *OH combines with the dehydrogenated intermediates adsorbed on the Pd sites to form GA. COHP calculations (Fig. 6d) show that the introduction of Ag enhances the stability of C-C bonds and weakens O-H bonds, therefore inhibiting C-C bond cleavage and ensuring the preservation of GA skeleton. Importantly, the optimized PdAg/NF only require 0.57 V vs. RHE to achieve 10 mA cm^{-2}, in addition to high faradic efficiency of up to 92% for GA production. And the current density can reach up to 300 mA cm^{-2} without oxygen evolution, suggesting the potential for large quantity GA production[55].



Just Accepted

Figure 6 (a) XRD patterns of PdBi, Bi, and Pd powders scraped from the NF substrate. (b) Pd 3d XPS spectra of PdBi/NF and Pd/NF. (c) EGOR performance study of PdBi/NF, Pd/NF, and Bi/NF. (d) Crystal orbital Hamiltonian population analysis of intermediate adsorbed on Pd (111) and PdAg (111) surfaces. (a)-(c) Reproduced with permission.[48] Copyright *2025 Wiley-VCH GmbH.* (d) Reproduced with permission.[55] Copyright *2021 Elsevier Inc.*

Xingye Lu et al. designed PtPd NPs anchored on $Ni(OH)_2$ support (PtPd-$Ni(OH)_2$) electrocatalysts [90], reaching 1 A cm^{-2} at 1.24 V vs. RHE and with high stability for over 700 h, which far outperforms the monometallic counterparts (Pt-$Ni(OH)_2$ and Pd-$Ni(OH)_2$). Additionally, high GA selectivity of 90.3% is achieved at an applied potential of 0.7 V vs. RHE. After alloying, Pd demonstrates a positive shift in valence state, which could facilitate the adsorption and activation of hydroxyls and reactants. Much less Pd dissolution after stability test is also observed compared with Pd-$Ni(OH)_2$. In-situ characterizations and DFT calculations further confirms the favorable EG adsorption and sufficient *OH species supply around the PtPd sites, which ultimately lowers the free energy barrier for the rate-determining step for $*COCH_2OH$ conversion to $*HOOCCH_2OH$[70].

3.3 Strain Engineering

Strain engineering modulates atomic spacing and orbital overlap to tune the electronic structure and d-band center of EGOR catalysts. Such tensile or compressive strain can arise from alloying-induced lattice changes, lattice mismatch at heterointerfaces, or core-shell architectures[91]. Because interfacial strain gradually relaxes away from the interface, active surfaces must remain close to the strained region, commonly through ultrathin shells of fewer than six atomic layers or cluster-support structures[92]. In catalyst design, this can be achieved by introducing new phases during synthesis [90] or by artificially combining two intrinsically different materials to create lattice mismatch, thereby optimizing catalytic performance.

Han Wang et al. [52] designed a model catalyst featuring lattice-distorted Pd (l-Pd) through strong electronic metal-support interactions (EMSI). The strong metal-support interaction between Pd and the substrate induces strain in the Pd lattice, which significantly drive electron delocalization on the metal surface, generating electron-deficient Pd sites, strongly attracting OH^- through electrostatic interaction, leading to the enhanced *OH adsorption on Pd. The lattice spacing increased from 2.26 Å for p-Pd to 2.30 Å for l-Pd, confirming lattice strain on the l-Pd surface, corresponding to approximately 1.8% lattice expansion (Fig. 7a). Geometric phase analysis (GPA) revealed significant in-plane tensile strain (E_{xx}) and shear tensile strain (E_{xy}) in l-Pd compared to p-Pd (Fig. 7b). EDS elemental mapping confirmed the uniform distribution of Pd, Ni, and O elements (Fig. 7c), and Pd maintained its NP morphology without extensive aggregation. These results sufficiently verify that the strong metal-support interaction (EMSI) between Pd and NiO_x can induce significant lattice distortion during spontaneous redox processes. According to the integrated crystal orbital Hamilton population (ICOHP) values (Fig. 7d), the Pd-O bond strength on l-Pd (ICOHP = -0.15 eV) is considerably stronger than that on p-Pd (ICOHP = -0.04 eV), indicating enhanced Pd-O orbital overlap. This suggests that electron-deficient Pd strongly attracts OH^- anions via electrostatic interaction, leading to an enhanced concentration of *OH adsorbed on the Pd surface. Abundant surface *OH coverage is crucial for weakening the adsorption of $*COCH_2OH$ or other carbonyl intermediates and promoting C-H bond oxidation, thereby substantially inhibiting surface poisoning and synergistically promoting the generation of GA. DFT calculations demonstrated (Fig. 7e) that throughout EGOR process, l-Pd exhibits the lowest energy barrier, with a rate-determining step (RDS) energy of 0.87 eV, significantly lower than the 1.51 eV for p-Pd. Specifically, l-Pd delivers a current density of 300 mA cm^{-2} at an ultralow potential of 1.03 V vs RHE, while achieving a maximum GA FE of 98.3% and a selectivity of 92.8% at 0.8 V vs. RHE. In sharp contrast, p-Pd exhibited a GA selectivity of only 50.1% and a FE of only 62.7%.

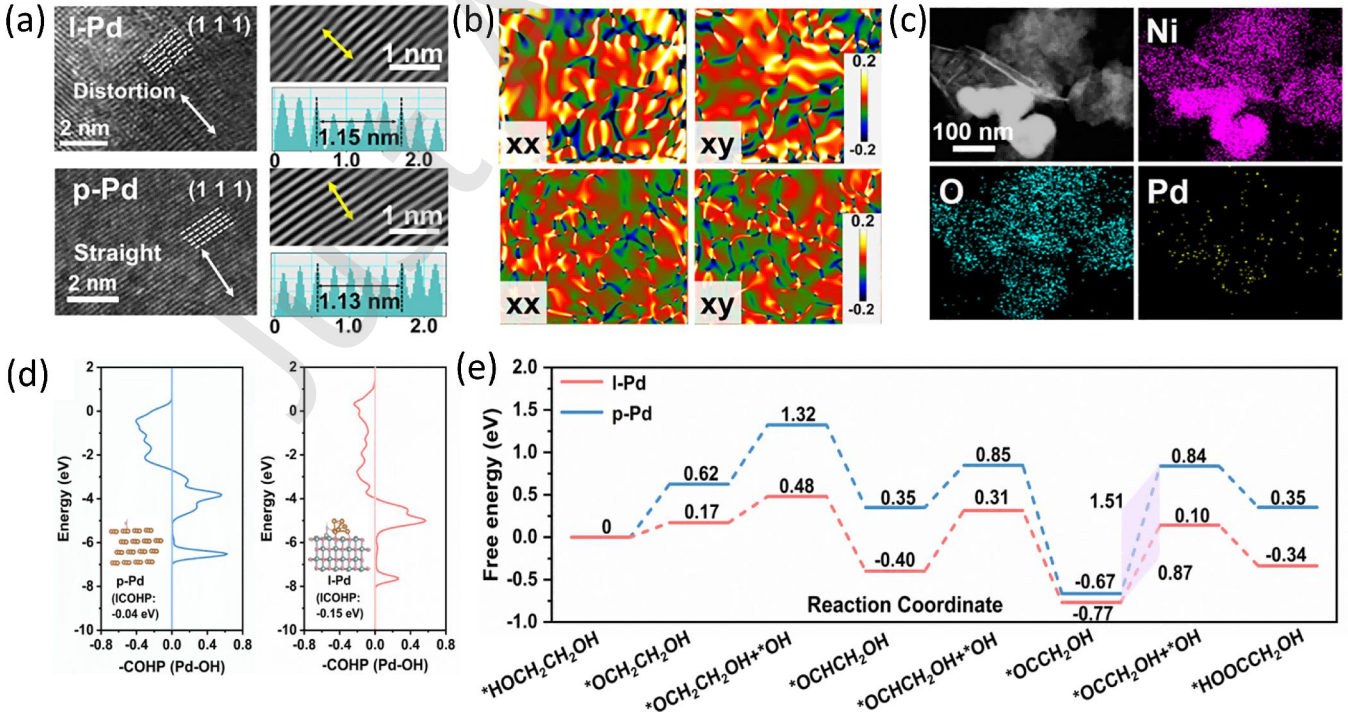


Figure 7 (a) IFFT images and corresponding lattice spacing of l-Pd and p-Pd. (b) In-plane strain tensor maps (E_{xx} and E_{xy}) for l-Pd and p-Pd (regions from green to dark blue denote compressive strain, while those from red to bright yellow correspond to tensile strain). (c) EDS elemental mapping images of l-Pd. (d) COHP analyses of *OH adsorption on p-Pd and l-Pd. (e) Gibbs free energy diagrams for EG-to-GA oxidation on p-Pd and l-Pd. (a)-(e) Reproduced with permission.[52] Copyright *2026 American Chemical Society.*

Just Accepted

Tensile strain can also be applied by constructing heterophases. Feng et al. reported thiol-modulated mesoporous PtPbBi nanosheets with an alloy/intermetallic compound heterophase, generating ~3% tensile strain from the interphase lattice mismatch, leading to a high EGOR mass activity of 10.6 A mg^{-1} and a low cell voltage of 0.58 V at 10 mA cm^{-2} for EG-assisted water splitting with stable operation over 200 h in AEM electrolyzer. DFT calculations further verify this tensile strain upshifts the Pt d-band center, and along with the introduction of thiols, to facilitate the EG and *OH adsorption, leading to enhanced kinetics.

3.4 High-Entropy Engineering

High-entropy alloys (HEAs), typically comprising five or more elements at 5-35%, and related multicomponent catalysts provide broad compositional flexibility and diverse potential active sites for EGOR[93], leading to a variation of adsorption energies, which is particularly important for the multistep process (EG adsorption, hydroxyl activation, intermediate conversion, and product desorption) involving a series of intermediates[94]. In addition to the diverse active centers and "cocktail" effects that could enhance the catalytic activity [95], lattice-potential fluctuations could also suppress atomic migration and improve structural stability through the sluggish-diffusion effect[96, 97].

Qingshou Zheng et al. [57] synthesized Ir-doped PdPtAuNiCu high-entropy alloy nanoparticles. The multi-site synergy of non-noble metal elements endows the HEAs with a refined electronic structure while reducing the usage of noble metals[57]. XRD patterns and elemental mapping (Fig. 8a, b) confirmed the successful synthesis of the high-entropy nanoparticles. Fig. 8c reflects the adsorption status within the inner Helmholtz layer. The initial OCP values for Ir-PdPtAuNiCu, PdPtAuNiCu HEANs, and Pt/C in the NaOH electrolyte were 1.002, 0.978, and 0.954 V vs. RHE, respectively. Upon EG injection, the OCP values of all three catalysts decay significantly following the order: Pt/C (~0.628 V) > Ir-PdPtAuNiCu (~0.618 V) > PdPtAuNiCu (~0.579 V). This trend aligns with their adsorption strength for EG and OH^-, originating from the variations in their d-band centers. Fig. 8d further investigates OH^- adsorption capability. Ir-PdPtAuNiCu displays a broad and distinct OH^- adsorption peak at ~0.8 V vs. RHE, whereas the corresponding adsorption peaks for PdPtAuNiCu and Pt/C are significantly weaker. Importantly, LSV results (Fig. 8e) further confirms the higher EGOR activity for Ir-PdPtAuNiCu compared with the PdPtAuNiCu and Pt/C control groups.

Xiaoyang Fu et al. [95] prepared multicomponent Au-doped PtAgRuCu wavy nanowires (WNWs), in addition to the cocktail effect, the one-dimensional defect-rich morphology could benefit charge transport and introduce additional active sites. Collectively, the Au-doped PtAgRuCu WNWs demonstrated ultrahigh mass activity of 23.2 A mg^{-1} for EGOR. Moving one step further, in the MEA device, only 0.57 V is required to achieve 100 mA cm^{-2} without any iR compensation, in addition to robust operation and nearly 100% FE for GA production, which further confirms the stability and selectivity of the Au-doped PtAgRuCu WNWs electrocatalysts.

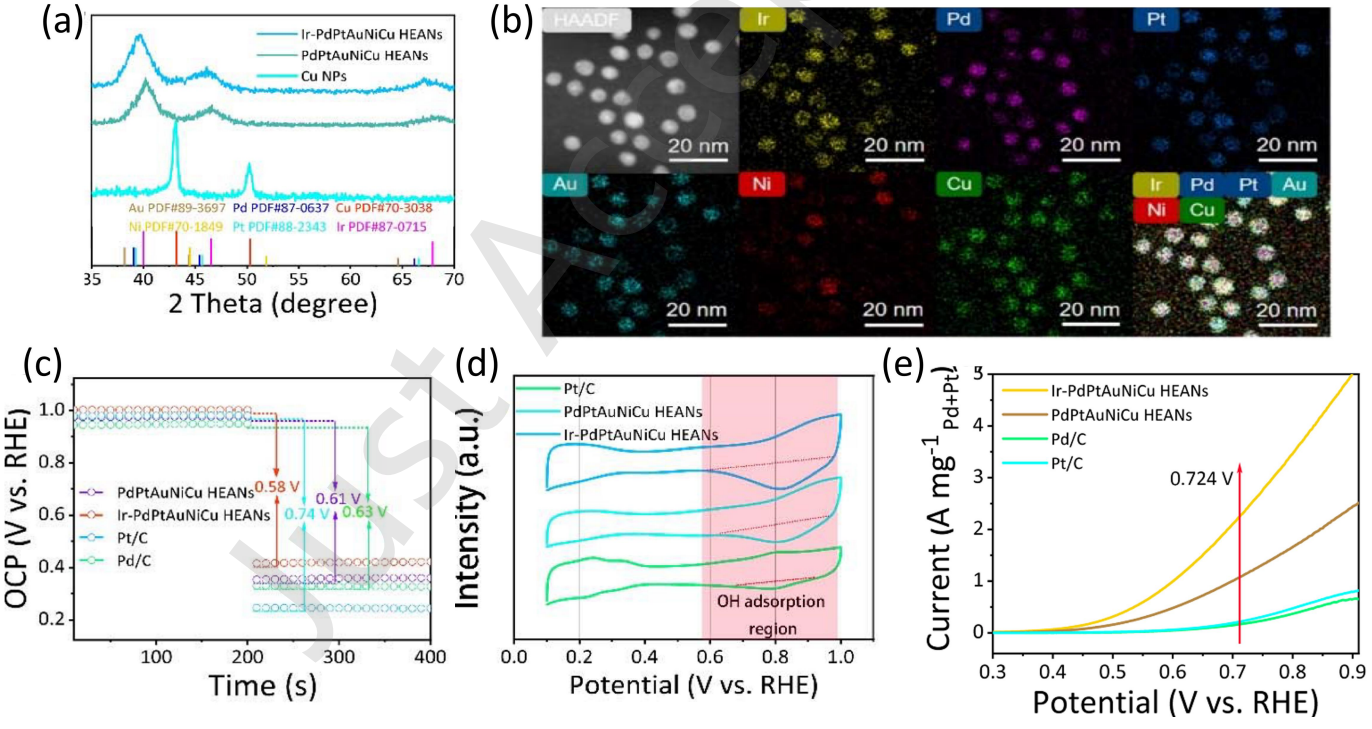


Figure 8 (a) XRD patterns of Ir-PdPtAuNiCu HEANs, PdPtAuNiCu HEANs, and Cu nanoparticles. (b) Elemental mapping of Ir-PdPtAuNiCu HEANs. (c) OCP of Ir-PdPtAuNiCu and PdPtAuNiCu HEANs and Pd/C and Pt/C catalysts. (d) Alkaline CV curves of Ir-PdPtAuNiCu, PdPtAuNiCu HEANs, and Pt/C catalysts. (e) LSV curves of Ir-PdPtAuNiCu HEANs, PdPtAuNiCu HEANs, and the commercial Pt/C and Pd/C in 1 M NaOH + 0.5 M EG at a scanning rate of 5 mV s^{-1}. (a)-(e) Reproduced with permission.[57] Copyright *2025 The Royal Society of Chemistry.*

4 Electrooxidation of Ethylene Glycol to Formic Acid/Formate

The selective oxidation of EG to formate proceeds through a six-electron C1 pathway involving stepwise *OH-assisted oxidation and dehydrogenation, and subsequent C-C bond cleavage of *$HOOCCH_2OH$ or *$OHCH_2CHO$ intermediates[98]. Theoretical calculations on Pt(111) revealed activation barriers of 0.57, 0.79, and 2.48 eV for O-H, C-H, and C-C bond cleavage, respectively, identifying C-C scission as the major kinetic challenge[99]. Accordingly, formate-selective catalysts should promote EG adsorption, dehydrogenation, *OH generation, C-C cleavage, and formate desorption, while suppressing OER and overoxidation to carbonate. Distortion, reconstruction, defect,

Just Accepted

and high-entropy engineerings can address these requirements by regulating electronic structure, generating dynamic active phases and coordination-unsaturated sites, and creating various potential multicomponent synergy.

For Non-noble-metal catalysts, particularly Ni and Co based materials, generally favor the C1 pathway because they readily reconstruct into high-valence oxyhydroxide active phases under anodic conditions. These species promote deep dehydrogenation and oxidation of EG-derived intermediates, strengthen the interaction with reactive OH/oxygen species, and facilitate C-C bond cleavage, thereby shifting the reaction toward formate formation [14, 46, 63, 65].

4.1 Distortion Engineering

Distortion engineering regulates EGOR by introducing deviations from ideal coordination geometries, thereby modifying metal-oxygen bond lengths, orbital splitting, covalency, and the electronic states near the Fermi level to further modulate the kinetics. Under alkaline EGOR conditions, variations in crystal structure, valence state, coordination environment, and morphology can generate distorted NiO_6 or CoO_6 units and NiOOH-related active motifs[100-106]. These local distortions regulate the energy and occupancy of e_g-derived states, thereby optimizing *OH and intermediate adsorption and lowering the barrier for C-C bond cleavage. For NiOOH-based catalysts, catalytic activity has been associated with the synergy between surface NiOOH and the precursor matrix[105], dopant-modified coordination environments[106], and distorted interfacial NiO_6 units[61]. Therefore, controlling local lattice distortion and coordination structure provides an effective strategy for improving EGOR activity and formate selectivity.

It is widely accepted that the electronic states near the Fermi level of a catalyst significantly influence its catalytic performance[107], Hui Luo et al.[108] proposed that the broadening of the e_g* band near the Fermi level facilitates electron transfer, ultimately enhancing catalytic activity. Zhen Wang et al.[46] synthesized Ni-based layered double hydroxide (LDH) catalysts (Ni_xMn_{1-x}LDH). As shown in Fig. 9a, Mn doping induces distortion of the NiO_6 octahedra. As the degree of octahedral distortion increases, the EGOR activity and the FA selectivity improves concurrently (Fig. 9b). The distortion-induced splitting of the e_g* orbitals raise the energy of the $d_{x^2-y^2}$ orbital while lowering that of the d_{z2} orbital, lifting their degeneracy. This reordering of orbital energy levels (Fig. 9c) directly modifies the electronic structure of the Ni sites. Broadening the e_g* band effectively increases the projected density of states (PDOS) near the Fermi level and upshifts the e_g* band center (Fig. 9d), enhancing the adsorption capacity for the glyoxal intermediate. Furthermore, this enhanced adsorption suppresses the Cannizzaro reaction associated with GA formation. Concurrently, Bader charge analysis reveals that e_g* band broadening reduces the electron density on the C atoms in glyoxal, weakening the C-C bond strength and promoting C-C bond cleavage. Consequently, the selectivity for formic acid is significantly improved.

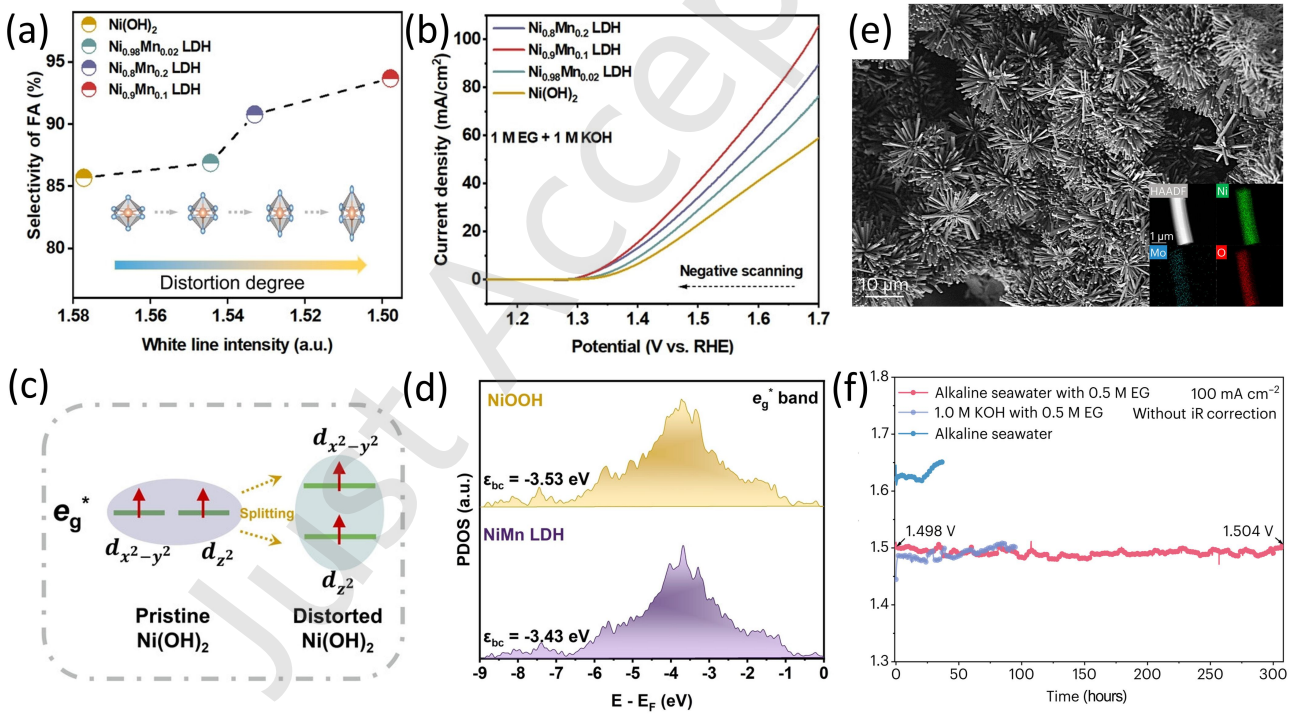


Figure 9 (a) The correlation between structural distortion and product selectivity. The stronger distortion (larger broadening of the e_g * band) leads to a higher formate selectivity. (b) Electrocatalytic activity of $Ni(OH)_2$-based catalysts in EGOR process. The linear sweep voltammetry (LSV) curves of synthesized Ni_xMn_{1-x} LDH (x=0.8, 0.9, 0.98) and $Ni(OH)_2$ in 1 M EG with 1 M KOH solution. (c) Schematic diagram of e_g * band splitting induced by NiO6 distortion. (d) Projected density of states for the e_g* band on NiOOH and NiMn LDH. (e) SEM image of Mo-$Ni(OH)_2$. Inset shows the energy--dispersive spectroscopy elemental mapping images of Mo--$Ni(OH)_2$. (f) Chronopotentiometry (CP) test in 1.0 M KOH with 0.5 M EG and alkaline seawater with/ without 0.5 M EG. (D) Comparison of EGOR activity with recently reported non-noble metal catalysts. HAADF, high angle angular dark field. (a)-(d) Reproduced with permission.[46] Copyright *2024 Wiley-VCH GmbH.* (e)-(f) Reproduced with permission. [47] Copyright *2025 The American Association for the Advancement of Science.*

Zehao Xiao et al.[47] prepared self-supported Mo-$Ni(OH)_2$ nanorods electrocatalysts on nickel foam (Fig. 9e). And selected-area electron diffraction reveals typical lattice mismatching of the amorphous phase, which could substantially induce lattice distortion. Importantly, the Mo-$Ni(OH)_2$ electrocatalysts demonstrate outstanding robustness with negligible performance decay over 300 hours under a current density of 100 mA cm^{-2} (Fig. 9f), and the activity also surpasses

Just Accepted

most of existing non-noble metal catalysts. Additionally, Mo incorporation creates the frustrated Lewis pairs featuring the electron-donating Mo and the electron-accepting Ni, which effectively combines spatially incompatible electron acceptors with donors, promoting charge redistribution, and could optimize the EG adsorption and FA desorption as well as the C-C bond cleavage. Moreover, DFT calculations further revealed that the C-C bond was elongated to 1.523 Å on Mo-Ni$(OH)_2$, in agreement with the promoted kinetics for C1 pathway.The high-performance liquid chromatography (HPLC) demonstrates that the highest faradic efficiency (FE; 95.8%) with selectivity (97.7%) is obtained at 1.55 V versus RHE .

4.2 Reconstruction Engineering

In the EGOR process, anode catalysts typically undergo reconstruction, leading to the formation of the corresponding metal oxides and oxyhydroxide[109, 110]. These reconstructed anode catalysts often exhibit distinct reaction kinetics and reaction pathways[111]. Moreover, previous studies have found that transition metal nitride, phosphide and sulfide-based catalysts undergo structural reconstruction during the EGOR process, with the generated metal (oxy)hydroxides playing a key role in determining catalytic performance[23, 66, 112-114]. A Ni substrate can form NiOOH via oxidative reconstruction on the catalyst surface, which acts as OH^-adsorption and activation sites to generate *OH, thereby preventing the adsorption of intermediates and promoting EG oxidation[62, 68, 115].

Transition metal phosphides (TMPs) have emerged as a new family of catalysts due to their metal-like properties, which combine good electrical conductivity and electrochemical stability when integrated with conductive substrates[116-119]. Recently, CoP has also been reported to exhibit high activity for the EGOR, highlighting its significant potential in various electrochemical applications. The positively charged Co sites can act as hydroxyl acceptors, while the P sites can facilitate the formation of high-valence Co during the OER[120, 121]. Despite these inherent advantages, the pristine catalytic performance of CoP remains far from satisfactory. A popular strategy involves heteroatom modification of the metal sites to modulate the electronic structure and surface properties of CoP, thereby favoring substrate activation and the adsorption of various intermediates[66].

Hua Zhou et al.[23] synthesized $CoNi_{0.25}P$ precatalyst, which undergoes complete reconstruction during EGOR, transforming into a low-crystallinity metal oxy(hydroxide) phase ($CoNi_{0.25}O_x(OH)_y$) which is the real active site. (Fig. 10a-c). This reconstructed product was confirmed to be the active center for the EGOR. Its high catalytic activity with a formate yield exceeding 80%, originates from the formation of unsaturated coordination of the metal sites after reconstruction. These sites efficiently cleave the C-C bond of EG and enable its selective conversion. XANES characterization (Fig. 10d) shows that the oxidation state of Co after reconstruction is predominantly +3, with spectral features closely matching those of the $CoNi_{0.25}OOH$ reference sample. The stability of $CoNi_{0.25}P$/NF was evaluated at a constant potential of 1.7 V vs. RHE for 39 h and 1.5 V vs. RHE for 33 h in HER||EGOR system. Within a broad potential window of 1.3-1.7 V vs. RHE, the formate selectivity remained above 90%, with a maximum Faradaic efficiency for formate of 91.7%. This performance was markedly superior to that of Pt/C, for which glycolic acid was the major product with an FE of 68.8%, and NiFe-LDH/NF, which exhibited a relatively low efficiency for C-C bond cleavage.[23].

The ordered macroporous superstructure of CoP with atomic-level Ni modification[66] represents an advanced design of CoP-based doping-reconstruction catalysts, exhibiting excellent catalytic performance due to its unique structural and electronic modulation mechanisms. Ni doping and reconstruction synergistically optimize the electronic structure. The substitution of Co sites by Ni atoms promotes electron transfer from electron-rich Ni to electron-deficient Co and P (Fig. 10e, f). This modulates the electronic distribution of CoP. Simultaneously, electrochemical reconstruction occurs during the EGOR, generating an Ni_1-CoOOH active phase and the introduction of Ni further promotes the formation of high-valence Co-O active species, enhancing EG dehydrogenation and C-C bond cleavage capabilities.

Just Accepted

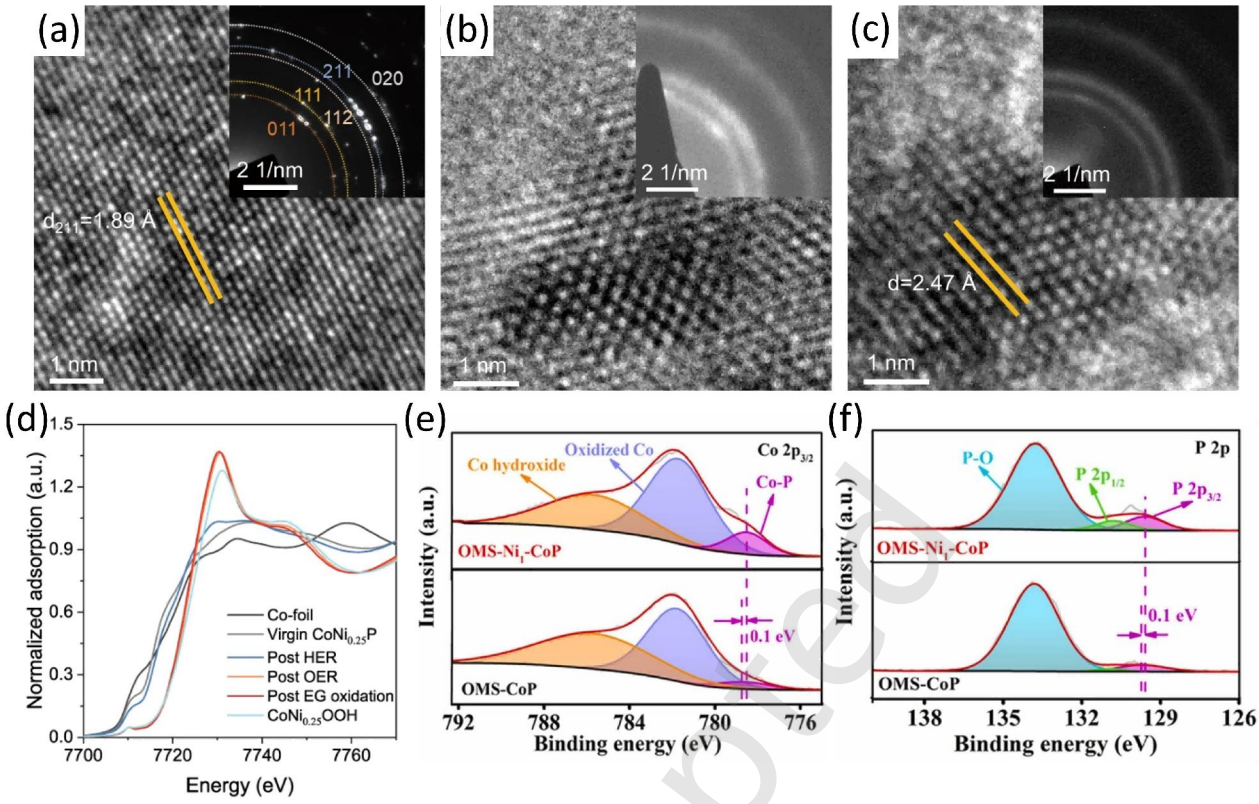


Figure 10 (a)-(c) TEM images and corresponding SAED patterns of CoNi0.25P after HER (a), OER (b), and EG oxidation (c) for 1 h. (d) Co K-edge XANES profiles. (e) High-resolution Co 2p spectra. (f) High-resolution P 2p spectra. (a)-(d) Reproduced with permission.[23] Copyright 2021*The Author(s). (e)*-(f) Reproduced with permission.[66] Copyright *2022 Elsevier B.V. All rights reserved.*

Xuan Liu et al.[67] synthesized Co-Ni_3N/CC, which could reconstruct to Co-Ni_3N@NiOOH/CoOOH core-shell structure. After the introduction of Co, the Ni^{2+}/Ni^{3+} redox behavior is enhanced, thereby promoting the formation of Ni^{3+} active sites and successfully lowers the EG oxidation potential to 1.15 V vs. RHE and overcoming the high potential limitation of traditional simple nickel-based catalysts. DOS calculations show that Co-Ni_3N exhibits higher electronic conductivity near the Fermi level. Additionally, strong charge exchange occurs among Ni, N, and Co, and the electronic redistribution at the interface facilitates the formation of surface catalytic groups active for both HER and EGOR.

Jinyong Sun et al.[14] prepared a CoNiOOH-Ni_3S_2/NF heterostructured electrocatalyst featuring an amorphous/crystalline interface. The heterointerface formed through such reconstruction serves as the active site for the catalytic reaction. At this interface, electron transfer from Ni_3S_2 to CoNiOOH shifts the d-band center toward the Fermi level, increasing the proportion of unoccupied antibonding orbitals and enhancing the adsorption capacity for reaction intermediates (*EG and *OH) [14]. The primary oxidation pathway involves two-step dehydrogenation of EG to GA, followed by *OH-assisted C-C bond cleavage of GA to generate a formaldehyde intermediate, which is further oxidized to formic acid. The adsorption energy of *EG is reduced to a greater extent than that of *OH, preventing site occupation by a single species and promoting synergistic reactions. Similarly, Yi Ma et al.[65] achieved surface reconstruction in alkaline media to form a NiCoOOH active layer, constructing a synergistic interface with Co_9S_8. This interface, which serves as the active site, significantly reduces the reaction barriers for the C-C cleavage step decreasing from 1.38 eV to 0.02 eV, and the rate-determining step (HCOOH* desorption) from 3.46 eV to 1.13 eV. Simultaneously, Co_9S_8 optimizes the electronic structure, concentrating the d-band center of Ni near the Fermi level, promoting interfacial charge redistribution, suppressing side reactions, and achieving a formate Faradaic efficiency of 92%[65].

4.3 Defect Engineering

Defect engineering is a strategy to enhance catalytic performance by increasing the number of active sites while simultaneously regulate the coordination environment and oxygen chemistry of EGOR catalysts. Oxygen vacancies, cation vacancies and under-coordinated metal centers can create adsorption sites for EG and *OH, and modulate the free energy and reactivity of surface oxygen-containing species. For formate-selective EGOR, these low-coordination environments are potentially valuable because they can promote the adsorption and activation of EG-derived C2 intermediates while lowering the energy barrier for C-C cleavage[122, 123].

Defect engineering also provides an effective platform for stabilizing isolated platinum-group metal atoms at vacancies or under-coordinated sites. This approach combines the strong C-C bond-cleavage capability of platinum-group metals with maximized atomic utilization, thereby reducing the noble-metal loading and catalyst cost[82]. The resulting defect-stabilized single-atom sites possess well-defined, low-coordination environments that can regulate the adsorption and activation of EG-derived intermediates. Consequently, single-atom sites can achieve high activity, selectivity, and durability at ultralow noble-metal loadings[124-127]. Minwei Song et al.[35] reported on EGOR catalysts based on Pt-group noble metals, noting that these metals all exhibit considerable activity for EGOR (Fig. 11a). The single-atom $Pt_1/Ni(OH)_2$-3 electrocatalyst demonstrates the best catalytic performance, achieving a high Faradaic efficiency and selectivity above 90% at 1000 mA cm^{-2} and 1.444 V vs. RHE. In contrast, commercial Pt/C exhibited an FE of only 53.8%, whereas the corresponding FE was

Just Accepted

approximately 1.7-fold higher for the catalyst under comparison. Aberration-corrected high-angle annular dark-field scanning transmission electron microscopy (AC HAADF-STEM) confirmed that Pt was uniformly distributed as single atoms rather than nanoparticles or clusters (Fig. 11b)[35]. To further evaluate the chemical state and local structure of $Pt_1/Ni(OH)_2$, Pt L_3-edge X-ray absorption near edge structure (XANES) spectroscopy (Fig. 11c) reveals the positive charge state of the Pt single atoms in the $Pt_1/Ni(OH)_2$-3 electrocatalyst compared to Pt foil [35] . The Pt single atoms form Pt-O-Ni bonds with the $Ni(OH)_2$ support, with an average valence state of +2.38 through electron transfer, which could enhance EG adsorption energy, and promoting O-H and C-H bond cleavage. DFT calculations showed that the d-band center of the Pt single-atom sites is closer to the Fermi level, improving electron transfer efficiency. Compared to commercial Pt/C and $Ni(OH)_2$, the $Pt_1/Ni(OH)_2$-3 catalyst exhibits a lower reaction energy barrier. Specifically, in the step of $*CH_2OHCHO$ conversion to $*CH_2OHCO$, the free energy barrier is significantly reduced, facilitating C-C bond cleavage and improving reaction kinetics.

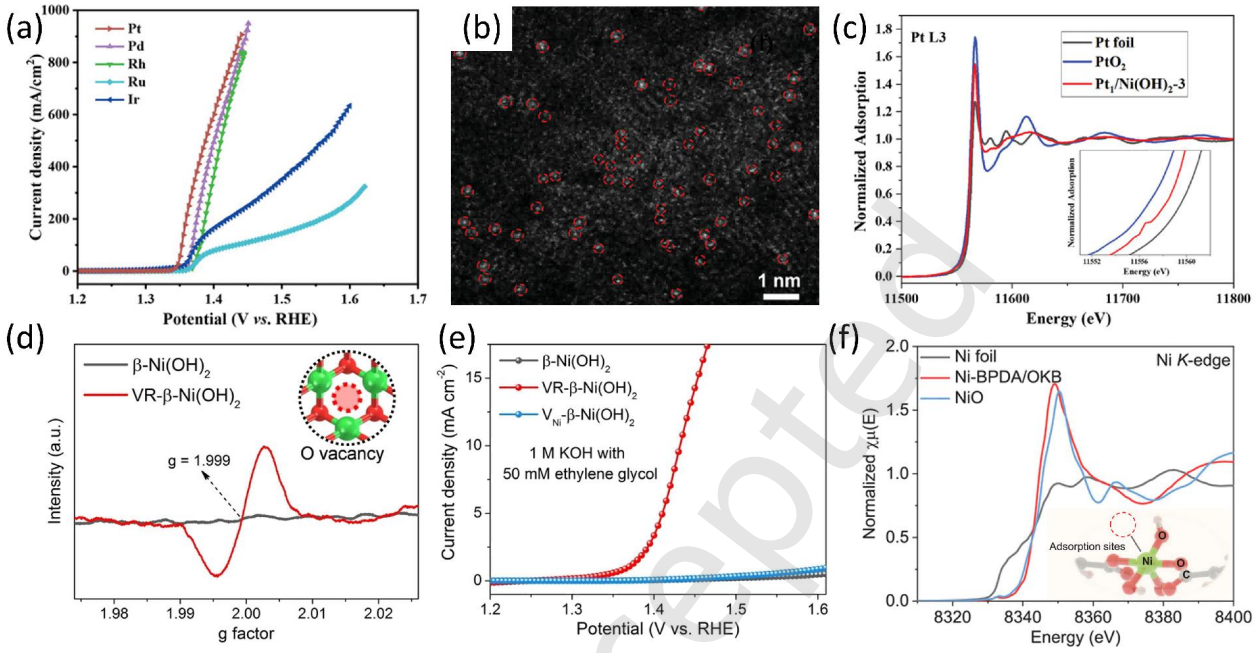


Figure 11 (a) LSV curves for noble metal synthesis electrocatalyst. (b) Aberration-corrected HAADF-STEM image of $Pt_1/Ni(OH)_2$-3 electrocatalyst. (c) Normalized Pt L3-edge XANES spectra of $Pt_1/Ni(OH)_2$-3 electrocatalyst. (d) EPR spectra of β-$Ni(OH)_2$ and VR-β-$Ni(OH)_2$. (e) Anodic polarization curves of β-$Ni(OH)_2$, VR-β-$Ni(OH)_2$, and V_{Ni}-β-$Ni(OH)_2$ in 1 M KOH with 50 mM ethylene glycol. (f) Normalized XANES spectra at the Ni K-edge of Ni-BPDA/OKB and structure of the catalyst. (a)-(c) Reproduced with permission. [35] Copyright *2024 Wiley-VCH GmbH.* (d)-(e) Reproduced with permission.[128] Copyright *2023 Wiley-VCH GmbH.* (f) Reproduced with permission.[62] Copyright *2025 Wiley-VCH GmbH.*

The lattice oxygen-mediated mechanism achieves alcohol dehydrogenation through hydrogen atom transfer (HAT) induced by immobile electrophilic lattice oxygen, but it cannot catalyze C-C bond cleavage[128]. Therefore, the oxygen vacancy-induced adsorbed oxygen-mediated mechanism (V_O-AOM) proposed by Wei Chen et al.[128] addresses the shortcomings of the LOM mechanism. NiO_xH_y species rich in oxygen vacancies expose coordinatively unsaturated Ni sites (V_O-Ni), promoting the generation of adsorbed electrophilic oxygen species (e. g., V_O-$Ni^{2+\delta}$-$(OH)_{ads}$). The selectivity for the HCOOH on V_O-β-$Ni(OH)_2$ is 97.2%.The EPR spectrum of V_O-β-$Ni(OH)_2$ in Fig. 11d shows a distinct symmetric oxygen vacancy EPR signal, confirming that V_O-β-$Ni(OH)_2$ possesses abundant oxygen vacancies[129, 130]. The lattice oxygen in the catalyst continues to be responsible for abstracting hydrogen atoms (HAT) from alcohol molecules via adsorbed oxygen, accelerating dehydrogenation. The high reactivity and mobility of the adsorbed oxygen directly attack the C-C bond, enabling the further oxidation to FA[128]. Nickel vacancies promote the formation of Ni^{3+}-O bonds (V_{Ni}-LOM-HAT), accelerating the dehydrogenation step, but do not participate in C-C bond cleavage. Compared to nickel vacancies, oxygen vacancy-containing catalysts exhibit significantly higher EGOR activity (Fig. 11e).

Zhijie Chen et. al. reported the strategy for synergistic regulation of cation doping and anion-vacancy formation, and prepared the Co, Cl co-doped Ni_3S_2 catalyst with improved EGOR performance [72]. Its interconnected ultrathin nanosheet architecture provides efficient pathways for mass transport and charge transfer. Owing to the higher electronegativity of Cl^- (3.16) than S^{2-} (2.58), the Ni/Co-Cl bonds are relatively weak and Cl^- can be preferentially substituted by OH^- or leached from the lattice under electrochemical conditions. This sacrificial removal of Cl^- promotes the generation of S vacancies and creates additional ion-transport channels within the catalyst. The resulting S-vacancy could produce coordinatively unsaturated Ni and Co sites, redistributes the local electron density, and strengthens the adsorption and activation of EG-derived intermediates. Meanwhile, Co doping shifts the d-band center upward and further optimizes the binding of reaction intermediates. The formation of S vacancies is also accompanied by an increase in the surface Ni^{3+}/Ni^{2+} ratio from 0.39 to 0.47, indicating that the defect-rich local environment favors the generation of high-valence Ni active sites. In addition, the enhanced covalency of the Ni-X bonds and the local structural perturbation around the defect sites facilitate interfacial electron transfer and improve the intrinsic activity of Ni centers. Therefore, the coupled effects of S-vacancy formation, coordinative unsaturation, and electronic modulation promote charge transfer, intermediate conversion, and C-C bond cleavage during EGOR. Defect engineering is also applicable to atomic active site. Chengdong Yang et al.[62] synthesized Ni-based molecular complexes by assembling Ni^{2+} ions BPDA on oxidized Ketjenblack (OKB), which further leads to the dynamic generation of coordinatively unsaturated Ni^{III}-OOH active sites, which could also be considered as a defective site. As shown by the Ni K-edge XANES spectra (Fig. 11f), the absorption edge and white-line feature of Ni-BPDA/OKB are markedly shifted

Just Accepted

relative to those of Ni foil and closely resemble those of NiO, indicating that the Ni centers in Ni-BPDA/OKB are positively charged and predominantly exhibit a Ni^{2+} like electronic state before electrochemical activation. This atomically exposed Ni sites can directly adsorb EG, activate the C-C bond through unoccupied Ni d orbitals, leading to an ultrahigh current density of 800 mA cm^{-2} at 1.59 V. The FE for formate during EG oxidation were all above 94%. Additionally, the proton abstraction from C-H bond will lead to the reversible redox from Ni^{III}-OOH to Ni^{II}-OH, and Ni-BPDA/OKB exhibits the highest π-π stacking energy between the Ni molecular complex and the carbon substrate, which facilitates electron transfer and the formation of high-valence Ni^{III}-OOH active site.

4.4 High-Entropy Engineering

High-entropy multicomponent materials, including carbides, oxides, and oxysulfides, provide diverse local coordination environments and chemically distinct active sites for the cooperative regulation of EG adsorption, *OH activation, intermediate conversion, and C-C bond cleavage. Their advantages arise not only from compositional complexity but also from the coordinated regulation of high-valence metal centers, oxygen vacancies, and reactive oxygen species, making them promising candidates for formate-selective EGOR.

Qiaoyi Xiang et al.[131] developed a phosphorus-doped high-entropy carbide supported on carbon nanofibers (P-HEC/CNFs), containing Fe, Co, Ni, Mn, Mo, and P. Ni^{3+} species were identified as the dominant active centers, promoting the spontaneous dehydrogenation of EG into alkoxy intermediates, followed by their oxidation to glyoxal-like species and subsequent C-C bond cleavage toward formate. Phosphorus doping redistributed the local electron density, strengthened EG adsorption, and stabilized high-valence Ni^{3+} sites. Consequently, P-HEC/CNFs exhibited a lower overpotential and higher formate selectivity than the undoped HEC.

This concept is further extended from the electronic regulation of metal centers to the control of oxygen species, Bolar et al.[132] introduced sulfur into a MnFeCoNiCu high-entropy oxide to form a sulfur-stabilized high-entropy oxysulfide. Covalent metal-sulfur interactions stabilized oxygen vacancies and high-valence transition-metal states, while promoting the cooperative involvement of lattice oxygen and adsorbed oxygen in C-C bond cleavage. Sulfur incorporation also accelerated hydrogen-atom transfer, resulting in efficient formate production with a Faradaic efficiency of 84.6%.

5 Summary and Outlook

The electrocatalytic oxidation of PET-derived EG represents a promising upcycling strategy to produce value-added GA or FA with energy-saving hydrogen production. Importantly, product selectivity is governed by the competing C2 and C1 oxidation pathways, thus, this review has elaborated the EGOR mechanism and summarized the electrocatalysts design strategies. For GA production through the C2 pathway, selective oxidation of one hydroxymethyl group is required while excessive C-C bond cleavage must be suppressed. Noble-metal catalysts such as Pt and Pd, especially when coupled with oxophilic components, have shown advantages in promoting OH^--assisted alcohol dehydrogenation, modulated intermediate adsorption, product desorption to improve activity, selectivity and stability through interfacial, alloying, strain and high entropy engineering. In contrast, FA production through the C1 pathway involves more thorough oxidation of EG and efficient C-C bond cleavage. Ni- and Co-based precatalyst could undergo in situ reconstruction into high-valent oxyhydroxide active phases for effective C-C bond scission. Additionally, distortion engineering, defect engineering and high entropy engineering can further regulate the electronic structure of active sites, optimize e_g orbital occupancy, modulate the adsorption of key intermediates, and facilitate C-C bond cleavage, thereby enhancing FA selectivity. Despite these advances, PET-derived EGOR still faces challenges in overall catalytic activity, long-term stability, and mechanistic elucidation, underscoring the need for accelerated discovery of efficient and selective catalysts. Accordingly, the following outlook discusses emerging opportunities in non-precious-metal catalyst design, dynamic potential modulation, advanced operando characterization, and AI-assisted catalyst discovery.

5.1 Non-Precious Metal Catalysts for the Oxidation of EG to GA

Compared with noble-metal catalysts, non-precious-metal catalysts for the selective oxidation of ethylene glycol to glycolate remain relatively underexplored, despite of their obvious cost advantages. This direction is particularly promising for the widespread practice of PET-derived EG upcycling, because transition-metal hydroxides, oxyhydroxides, oxides, and atomically dispersed metal-nitrogen-carbon catalysts offer rich redox chemistry, tunable metal-oxygen covalency, and flexible coordination environments[66]. However, achieving high glycolate selectivity on non-precious-metal catalysts is challenging. Under alkaline anodic conditions, many Ni-, Co-, and Fe-based catalysts tend to evolve into high-valent oxyhydroxide phases, which may promote excessive oxidation or C-C bond cleavage if the adsorption and conversion of C2 intermediates are not properly regulated. Therefore, the central challenge is to construct non-precious-metal active sites that can promote alcohol dehydrogenation and C2 oxygenate formation while suppressing overoxidation and C-C scission.

Recent progress in dual-atom catalysts provides a useful design concept. For example, Shuai Yue et al.[58] developed Ni_1-Fe_1-N-C dual-atom catalysts for EG oxidation, where the introduction of Ni sites significantly downshifted the d-band center of the Fe single site, thereby weakening the adsorption of the key CH_2 OHCO* intermediate on Fe[58]. This optimized configuration promoted timely glycolate desorption and suppressed further overoxidation. Meanwhile, the oxophilic Ni site facilitated *OH adsorption, accelerating intermediate conversion. This example highlights the potential of dual-site regulation in non-precious-metal catalysts, where one site controls C2 intermediate adsorption/desorption and the other assists *OH activation. Future efforts may focus on precisely tuning the electronic coupling, spatial distance, and coordination environment of such dual sites to balance EG activation, glycolate release, and suppression of C-C cleavage.

5.2 Dynamic Potential Strategies for Selectivity Control and Anti-Deactivation

Dynamic potential modulation provides an additional degree of freedom for regulating EGOR selectivity and catalyst stability. Unlike the conventional constant-potential or current operation, dynamic potential strategy (pulsed or cyclic) can periodically change the surface oxidation state, adsorbate coverage, and local reaction environment, thereby influencing the competition between C2-preserving oxidation, C-C bond cleavage, OER, and catalyst deactivation. This approach is particularly relevant for EGOR because many active surfaces undergo continuous oxidation, reconstruction, or poisoning by strongly adsorbed carbonyl and carboxylate intermediates during long-term electrolysis.

Fahao Ma et al.[71] designed a Pt@$Ni(OH)_{2-x}$ electrocatalyst composed of Ni-O-Pt interfaces and abundant oxygen vacancies, which successfully realized a smart switch between C-C bond-preserved products and C-C bond-cleavage products during the

electrooxidation of EG and glycerol, demonstrating that product selectivity can be tuned by controlling the surface redox state and oxygen-species chemistry via potential modulating.

Wei Chen et al.[133] employed a pulsed potential strategy to selectively oxidize glycerol to glyceric acid on Pt-based catalysts. In situ FT-IR and quasi in-situ XPS demonstrated the pulsed potential can modulate the oxidation state and surface structure of the catalyst, preventing the excessive accumulation of poisoning intermediates, thereby freeing active sites, and facilitating the adsorption of reactants and active species (*OH). Although demonstrated for glycerol oxidation, this strategy provides a transferable concept for mitigating noble-metal deactivation in EGOR.[133]. Gui Zhao et al.[59] reported Electrochemical Potential Cycling (EPC) strategy, by alternately adjusting the electrode potential between oxidative and reductive regions, noble metal surface deactivation was mitigated, leading to significantly enhanced the EG conversion rate by 20-fold while maintaining a GA selectivity of >95%. In situ Raman and X-ray absorption spectroscopy further confirms the efficient removal of surface oxides during the reaction process[59].

Future studies should move beyond empirical potential selection and establish quantitative relationships between potential sequence parameters and product distribution in addition to performance recovery. Important variables include upper and lower potential limits, pulse duration, frequency, duty cycle, total energy consumption, and compatibility with H-cell or MEA devices. Combining time-resolved operando spectroscopy with online product analysis will be particularly important for identifying how surface oxides, adsorbed C2 intermediates, and active oxygen species evolve during each potential cycle. Such understanding may enable programmable EGOR systems in which selectivity and anti-deactivation are simultaneously optimized through electrochemical waveform engineering.

5.3 Advanced In Situ and Operando Characterization

Advanced in situ and operando characterization techniques are essential for establishing direct correlations among catalyst structure, surface reconstruction, intermediate adsorption, and reaction pathways under realistic EGOR conditions. In situ ATR-SEIRAS and FTIR spectroscopy can identify oxygenated C2 intermediates and formate- or glycolate-related species[134-136], whereas Raman spectroscopy can monitor hydroxide-to-oxyhydroxide reconstruction and the evolution of metal-oxygen motifs[59, 69, 73]. Operando X-ray absorption spectroscopy provides information on oxidation states, local coordination environments, and metal-support interactions, while quasi-in situ XPS or electrochemical ambient-pressure XPS complements these techniques by probing potential-dependent surface chemical states[133, 137].

A major future challenge is to correlate these structural and spectroscopic signals with time-resolved product formation. Many mechanistic assignments in EGOR remain indirect because catalyst reconstruction, intermediate adsorption, and product generation often occur simultaneously. Therefore, operando spectroscopy should be coupled with potential-dependent product analysis, isotope labeling, and carbon-balance measurements. For example, isotope-labeled EG or water could help distinguish whether oxygen atoms in glycolate/formate originate from hydroxide, water, lattice oxygen, or adsorbed oxygen species. In situ or environmental electron microscopy may also provide valuable information on catalyst formation, surface restructuring, and interface evolution[138], although the direct application to liquid-phase EGOR remains technically challenging. Integrating these methods will be crucial for identifying the true active phase and clarifying whether glycolate or formate selectivity arises from specific adsorption geometries, reactive oxygen species, lattice oxygen participation, or dynamic surface reconstruction.

5.4 Model EG electrooxidation versus direct electrooxidation of real PET hydrolysates

Although mechanistic investigations of EGOR are commonly conducted in model electrolytes with well-defined EG and alkaline-electrolyte concentrations, direct electrooxidation of real PET hydrolysates involves additional complexities associated with both PET depolymerization and feedstock composition. Zhou et al. demonstrated direct electro reforming of PET hydrolysate after alkaline depolymerization and showed that the resulting electrolyte contains both terephthalate and EG-derived oxidation products. Importantly, practical PET waste may also contain polyolefins, poly(lactic acid) (PLA), and lipids, whose removal or conversion introduces additional species into the reaction system[23].The chemical composition of real PET hydrolysates can therefore differ substantially from that of a purified EG electrolyte. For example, Rojas-Luna et al. detected not only terephthalate and EG but also 1,4-butanediol in the hydrolysate of commercial PET[139]. Such additional organic components may participate in electrooxidation or compete with EG-derived species for surface active sites.In addition, the effective EG concentration in a real hydrolysate is governed by the efficiency of PET depolymerization rather than simply by the nominal electrolyte composition. Yu et al. directly compared EGOR on three-dimensional Ni foam using a PET hydrolysate and a pure EG solution. Although the PET hydrolysate exhibited a similar onset potential of approximately 1.37 V vs. RHE, its lower peak current was attributed to incomplete PET depolymerization. The authors therefore emphasized the importance of optimizing hydrolysis temperature, KOH concentration, and reaction time prior to electrolysis[140].

More importantly, the complex hydrolysate environment can alter both catalytic activity and durability. A recent direct comparison of AuCu nanodendrites in pure EG and actual PET hydrolysate showed a higher initial activity in the real hydrolysate but a slight deterioration in stability[141]. These observations indicate that catalyst performance obtained in purified pure EG and alkaline electrolyte cannot necessarily be extrapolated directly to practical PET hydrolysates.Nevertheless, direct PET-hydrolysate electrooxidation can maintain high product selectivity when the catalyst and reaction environment are appropriately designed. For example, $NiCu_{60s}$/NF achieved a formate FE of 95.8% in a model electrolyte containing 0.3 M EG and 1.0 M KOH. When commercial PET powder hydrolysate was used, the hydrolysate was deliberately diluted to 1.0 M KOH to minimize the influence of pH differences, and formate remained the sole oxidation product with an FE above 80% during 5 h electrolysis. More practically, when a commercial PET water-bottle hydrolysate was directly tested in 2.0 M KOH, despite its much lower EG concentration (7.96 mM), formate was still identified as the sole oxidation product, and EG was completely converted after 1 h electrolysis at 1.52 V vs. RHE, accompanied by the recovery of pure terephthalic acid. These results demonstrate that high product selectivity can be retained in realistic PET-derived electrolytes, but they also highlight that direct comparisons with model EG solutions must account for differences in alkalinity, effective EG concentration, and hydrolysate composition[64].

Therefore, the transition from model EG electrooxidation to practical PET electroreforming should be regarded as more than a simple change in feedstock. It introduces coupled effects from hydrolysis efficiency, substrate concentration, feedstock impurities, competitive adsorption, catalyst reconstruction and poisoning, product selectivity, and downstream separation. Future studies should therefore benchmark catalysts not only in well-defined EG electrolytes but also under realistic PET-

hydrolysate conditions, with particular attention to hydrolysate composition, impurity tolerance, long-term durability, product distribution, and process-level separation requirements.

5.5 Extension to Other Alcohols and Biomass-Derived Feedstocks

Beyond PET-derived EG, the mechanism-guided catalyst-design principles discussed in this review may also be extended to other low-cost alcohols and biomass-derived oxygenates. Glycerol is particularly attractive because of its low cost and abundant availability, while its electrooxidation can produce various value-added oxygenated chemicals, such as lactic acid, glyceric acid, dihydroxyacetone, and formate. Lactic acid is an important platform chemical for the production of biodegradable poly(lactic acid) (PLA) and is widely used in the food and pharmaceutical industries[142]; glyceric acid and its derivatives have potential applications in surfactants and biofunctional materials[143]; dihydroxyacetone is an important high-value C3 chemical widely used in sunless tanning cosmetics, with additional applications in the pharmaceutical and fine chemical industries[144].

Its electrooxidation similarly involves multiple dehydrogenation steps and competition between C-C bond retention and cleavage. Therefore, key concepts established for EGOR, including the regulation of reactive oxygen species, intermediate adsorption, oxidation depth, and C-C bond cleavage, may provide transferable guidelines for controlling the activity and product selectivity of glycerol oxidation. Recent progress in the electrooxidation of glycerol and other biomass-derived oxygenates further demonstrates the potential of extending these mechanism-guided strategies toward a broader range of sustainable feedstocks [145, 146].

5.6 Artificial intelligence-assisted discovery of EGOR catalysts

Traditional catalyst development has long relied on trial-and-error processes, which are time and resource intensive and often suffer from limited reproducibility. This problem becomes more pronounced in EGOR catalyst design because catalytic performance depends on a multidimensional parameter space involving catalyst composition, local coordination environment, surface reconstruction, electrolyte composition, EG concentration, applied potential, and product distribution. AI-assisted high-throughput screening offers a way to examine these variables more systematically by establishing quantitative preparation-structure-performance relationships [147]. In this context, high-throughput experimentation, density functional theory (DFT), automated characterization, and machine learning can be integrated into iterative workflows for catalyst optimization.

A key requirement for such studies is the construction of standardized EGOR datasets containing catalyst composition and structure, electrolyte composition, EG concentration, applied potential or current density, product-resolved Faradaic efficiencies, EG conversion, glycolate/formate yield, and long-term stability. Manual experiments can introduce operator-dependent variation and inconsistencies in data collection. Automated and self-driving laboratories can help reduce these variations while generating structured and machine-readable datasets [148-150]. Standardized data collection is also important for comparing results across different catalyst classes and operating conditions and for improving the transferability of machine-learning models.

At present, however, most AI-assisted catalyst studies still rely mainly on static preparation-structure-performance relationships, in which catalyst composition, structural descriptors, synthesis parameters, and end-point catalytic metrics are treated as model inputs and outputs. These data mainly describe the catalyst before or after reaction and do not fully capture the evolution of the catalyst surface under electrochemical operating conditions. This issue is relevant to EGOR because surface reconstruction, oxidation-state changes, local coordination environments, reactive oxygen species, intermediate adsorption, and active-site populations may all change with applied potential and reaction time.

In situ and operando characterization can provide experimentally grounded descriptors of these changes. Operando spectroscopies, rather than being used only for post hoc structural interpretation, can directly describe the catalytic state under working conditions. Time-resolved measurements may further provide descriptors such as reconstruction onset potentials, rates of active-phase formation, persistence of reaction intermediates, and changes associated with catalyst deactivation.

These operando-derived descriptors contain information that is not available from conventional static structural parameters. More importantly, they can be correlated with current density, Faradaic efficiency, and product distribution, allowing catalyst state to be connected directly with catalytic output. Machine learning has already been combined with operando spectroscopy to distinguish coexisting active-site configurations, follow catalyst restructuring, and identify adsorbate-dependent electronic and geometric states in electrocatalytic OER and CO_2 reduction. Real-time spectroscopic feedback has also begun to be incorporated into autonomous reaction-optimization workflows [151-153]. These studies provide a useful basis for similar approaches in EGOR. Descriptors such as the fraction of high-valent Ni/Co species, coordination-number evolution, reconstruction degree, intermediate spectral fingerprints, and potential-dependent active-phase populations may help describe the competition between C2 retention and C1 cleavage.

Complementary to these experimentally grounded dynamic structural and mechanism-related descriptors, DFT calculations can provide physically interpretable information on intrinsic reaction energetics. Relevant EGOR descriptors include *OH adsorption/formation energy, EG and C2-intermediate adsorption energies, glycolate/formate adsorption and desorption energetics, C-C bond cleavage barriers, the d-band center, and metal-oxygen covalency. These quantities are closely related to reaction kinetics and pathway competition. Favorable EG activation, appropriate *OH availability, suppressed C-C bond cleavage, and facile glycolate desorption generally favor the C2 pathway, whereas stronger activation of oxygenated intermediates and lower C-C cleavage barriers promote deeper oxidation toward formate. Coupling DFT with machine learning can therefore convert these mechanistic descriptors into predictive models [154, 155]. High-accuracy DFT calculations may first be performed for a representative subset of catalysts to construct training datasets, after which ML models can be used to estimate adsorption energetics and reaction barriers across a larger chemical space at lower computational cost. This approach enables EGOR screening to consider both activity and pathway selectivity rather than relying only on empirical composition-performance correlations.

From an algorithmic perspective, Bayesian optimization (BO) is useful for multicomponent catalyst systems with high-dimensional composition spaces, such as high-entropy alloys, for which exhaustive computation or experimentation is impractical. BO uses a probabilistic surrogate model to select the next experiments or calculations by balancing exploration and exploitation [156]. This is relevant to EGOR because catalyst design involves several objectives, including activity, glycolate/formate selectivity, long-term stability, and catalyst

Under review

cost. Multiobjective BO can therefore be used to identify Pareto-optimal catalyst compositions instead of optimizing only a single performance metric. Graph neural networks (GNNs), meanwhile, can represent catalysts as atomic graphs and learn relationships between local atomic environments and properties such as adsorption energies, intermediate binding strengths, and reaction barriers [157]. They may therefore be useful for defect-rich, reconstructed, and multicomponent EGOR surfaces.

The integration of operando characterization with AI also provides a way to move from static parameter optimization toward dynamic state-aware catalyst analysis. Conventional AI workflows mainly establish preparation-structure-performance relationships and search for favorable catalyst compositions. When time resolved and potential resolved descriptors are included, the model can additionally describe how a precursor evolves into the real active phase, how intermediate populations and surface states change during operation, and how these changes affect pathway switching and catalyst deactivation. The conventional preparation-structure-performance relationship can thus be extended to preparation-structure-state-performance correlations, with operando-derived descriptors linking material structure to catalytic output. Combining standardized experimental datasets, DFT-derived energetics descriptors, operando-derived structural and mechanism-related descriptors, machine-learning algorithms, and automated experimentation may eventually allow data-driven methods to evaluate not only catalyst composition but also the active states associated with activity, product selectivity, and long-term stability in EGOR.

Data availability

Not applicable.

Acknowledgements

X. F. acknowledges the support from the Beijing Natural Science Foundation (Z260003), China National Petroleum Corporation (CNPC) Innovation Found (2024DQ02-0212), the Fundamental Research Funds for the Central Universities, Peking University (Grant No. 7100604801) and State Key Laboratory of Advanced Waterproof Materials, Beijing Oriental Yuhong Waterproof Technology Co., Ltd. (SKLAWM-2025YJ06).

Declaration of competing interest

Not applicable.

Author contribution statement

Q. Qu: Data curation, methodology, validation, writing - original draft. X. Wang: Funding acquisition, project administration. C. Liu: Funding acquisition, project administration. Y. Feng: Data curation, methodology, validation, writing - review & editing. G. Han: Funding acquisition, project administration. R. Wang: Funding acquisition, project administration. Z. Wu: Funding acquisition, project administration. R. Yong: Funding acquisition, project administration. Z. Yang: writing - review & editing. X. Fu: Validation, funding acquisition, project administration, supervision, writing - review & editing. All the authors have approved the final manuscript.

Informed consent

Not applicable.

Ethics statement

Not applicable.

Use of AI statement

During the manuscript preparation, the authors employed GPT-5.5 for language polishing. Accordingly, the authors reviewed and edited the content and take full responsibility for the content.

References

[1] Chen, J.; Zhang, L.; Wang, L.; Kuang, M.; Wang, S.; Yang, J. Toward carbon neutrality: Selective conversion of waste plastics into value-added chemicals. *Matter* **2023**, *6* (10), 3322-3347. DOI: 10.1016/j.matt.2023.07.025.

[2] Coates, G. W.; Getzler, Y. D. Y. L. Chemical recycling to monomer for an ideal, circular polymer economy. *Nature Reviews Materials* **2020**, *5* (7), 501-516. DOI: 10.1038/s41578-020-0190-4.

[3] Stegmann, P.; Daioglou, V.; Londo, M.; van Vuuren, D. P.; Junginger, M. Plastic futures and their CO(2) emissions. *Nature* **2022**, *612* (7939), 272-276. DOI: 10.1038/s41586-022-05422-5.

[4] Geyer, R.; Jambeck, J. R.; Law, K. L. Production, use, and fate of all plastics ever made. *Sci Adv* **2017**, *3* (7), e1700782. DOI: 10.1126/sciadv.1700782.

[5] Bharadwaj, C.; Purbey, R.; Bora, D.; Chetia, P.; Maheswari R, U.; Duarah, R.; Dutta, K.; Sadiku, E. R.; Varaprasad, K.; Jayaramudu, J. A review on sustainable PET recycling: Strategies and trends. *Materials Today Sustainability* **2024**, *27*. DOI: 10.1016/j.mtsust.2024.100936.

[6] Wang, C.; Han, H.; Wu, Y.; Astruc, D. Nanocatalyzed upcycling of the plastic wastes for a circular economy. *Coordination Chemistry Reviews* **2022**, *458*. DOI: 10.1016/j.ccr.2022.214422.

[7] Han, S.; Wang, J.; Li, Y.; Wang, C.; Wu, Y.; Liu, B. Strategies for Electrochemical Recycling of Plastic Polyethylene Terephthalate‐Derived Ethylene Glycol Into High‐Value Chemicals. *Advanced Energy Materials* **2025**, *15* (34). DOI: 10.1002/aenm.202502368.

[8] Van Geem, K. M. Plastic waste recycling is gaining momentum. *Science* **2023**, *381* (6658), 607-608. DOI: 10.1126/science.adj2807.

[9] Zhang, S.; Zhao, X.; Liu, X.; Chen, L.; Bai, L.; Xu, S.; Wang, Y.-Z. Chemical depolymerization of polyethylene terephthalate and its blends: Enhanced strategies for efficient circularity. *Progress in Polymer Science* **2025**, *164*. DOI: 10.1016/j.progpolymsci.2025.101958.

[10] Jehanno, C.; Alty, J. W.; Roosen, M.; De Meester, S.; Dove, A. P.; Chen, E. Y.; Leibfarth, F. A.; Sardon, H. Critical advances and future opportunities in upcycling commodity polymers. *Nature* **2022**, *603* (7903), 803-814. DOI: 10.1038/s41586-021-04350-0.

[11] Zhang, Z.; Wang, J.; Ge, X.; Wang, S.; Li, A.; Li, R.; Shen, J.; Liang, X.; Gan, T.; Han, X.; et al. Mixed Plastics Wastes Upcycling with High-Stability Single-Atom Ru Catalyst. *J Am Chem Soc* **2023**, *145* (41), 22836-22844. DOI: 10.1021/jacs.3c09338.

[12] Shi, K.; Ren, Y.; Zhou, B.; Chen, L.; Shi, J. Electrocatalytic Alcohol Oxidation to Aldehyde Through Direct Dehydrogenation Mechanism Using a High-Performance Pt/Co(3)O(4) Catalyst. *Angew Chem Int Ed Engl* **2025**, *64* (51), e202518122. DOI: 10.1002/anie.202518122.

[13] Chen, J.; Zhang, F.; Kuang, M.; Wang, L.; Wang, H.; Li, W.; Yang, J. Unveiling synergy of strain and ligand effects in metallic aerogel for electrocatalytic polyethylene terephthalate upcycling. *Proc Natl Acad Sci U S A* **2024**, *121* (17), e2318853121. DOI: 10.1073/pnas.2318853121.

[14] Sun, J.; Shi, B.; Dai, S.; Chu, L.; Wang, H.; Huang, M. Promoted *OH Adsorption Facilitates C–C Bond Cleavage for Efficient Electrochemical Upcycling of Polyethylene Terephthalate. *ACS Catalysis* **2024**, *15* (1), 529-542. DOI: 10.1021/acscatal.4c05352.

[15] Chu, M.; Liu, Y.; Lou, X.; Zhang, Q.; Chen, J. Rational Design of Chemical Catalysis for Plastic Recycling. *ACS Catalysis* **2022**, *12* (8), 4659-4679. DOI: 10.1021/acscatal.2c01286.

[16] Santos, R. G.; Machovsky-Capuska, G. E.; Andrades, R. Plastic ingestion as an evolutionary trap: Toward a holistic understanding. *Science* **2021**, *373* (6550), 56-60. DOI: 10.1126/science.abh0945.

[17] Laldinpuii, Z. T.; Khiangte, V.; Lalhmangaihzuala, S.; Lalmuanpuia, C.; Pachuau, Z.; Lalhriatpuia, C.; Vanlaldinpuia, K. Methanolysis of PET Waste Using Heterogeneous Catalyst of Bio-waste Origin. *Journal of Polymers and the Environment* **2021**, *30* (4), 1600-1614. DOI: 10.1007/s10924-021-02305-

Just Accepted

0.
[18] Pham, D. D.; Cho, J. Low-energy catalytic methanolysis of poly(ethyleneterephthalate). *Green Chemistry* **2021**, *23* (1), 511-525. DOI: 10.1039/d0gc03536j.
[19] Jain, A.; Soni, R. K. Spectroscopic investigation of end products obtained by ammonolysis of poly (ethylene terephthalate) waste in the presence of zinc acetate as a catalyst. *Journal of Polymer Research* **2007**, *14* (6), 475-481. DOI: 10.1007/s10965-007-9131-9.
[20] Nunes, B. F. S.; Oliveira, M. C.; Fernandes, A. C. Dioxomolybdenum complex as an efficient and cheap catalyst for the reductive depolymerization of plastic waste into value-added compounds and fuels. *Green Chemistry* **2020**, *22* (8), 2419-2425. DOI: 10.1039/c9gc04206g.
[21] Kratish, Y.; Li, J.; Liu, S.; Gao, Y.; Marks, T. J. Polyethylene Terephthalate Deconstruction Catalyzed by a Carbon-Supported Single-Site Molybdenum-Dioxo Complex. *Angew Chem Int Ed Engl* **2020**, *59* (45), 19857-19861. DOI: 10.1002/anie.202007423.
[22] Furukawa, M.; Kawakami, N.; Tomizawa, A.; Miyamoto, K. Efficient Degradation of Poly(ethylene terephthalate) with Thermobifida fusca Cutinase Exhibiting Improved Catalytic Activity Generated using Mutagenesis and Additive-based Approaches. *Sci Rep* **2019**, *9* (1), 16038. DOI: 10.1038/s41598-019-52379-z.
[23] Zhou, H.; Ren, Y.; Li, Z.; Xu, M.; Wang, Y.; Ge, R.; Kong, X.; Zheng, L.; Duan, H. Electrocatalytic upcycling of polyethylene terephthalate to commodity chemicals and H(2) fuel. *Nat Commun* **2021**, *12* (1), 4679. DOI: 10.1038/s41467-021-25048-x.
[24] Li, Y.; Wang, M.; Liu, X.; Hu, C.; Xiao, D.; Ma, D. Catalytic Transformation of PET and CO(2) into High-Value Chemicals. *Angew Chem Int Ed Engl* **2022**, *61* (10), e202117205. DOI: 10.1002/anie.202117205.
[25] Yan, Y.; Zhou, H.; Xu, S. M.; Yang, J.; Hao, P.; Cai, X.; Ren, Y.; Xu, M.; Kong, X.; Shao, M.; et al. Electrocatalytic Upcycling of Biomass and Plastic Wastes to Biodegradable Polymer Monomers and Hydrogen Fuel at High Current Densities. *J Am Chem Soc* **2023**, *145* (11), 6144-6155. DOI: 10.1021/jacs.2c11861.
[26] Yue, H.; Zhao, Y.; Ma, X.; Gong, J. Ethylene glycol: properties, synthesis, and applications. *Chem Soc Rev* **2012**, *41* (11), 4218-4244. DOI: 10.1039/c2cs15359a.
[27] Du, M.; Zhang, Y.; Kang, S.; Xu, C.; Ma, Y.; Cai, L.; Zhu, Y.; Chai, Y.; Qiu, B. Electrochemical Production of Glycolate Fuelled By Polyethylene Terephthalate Plastics with Improved Techno-Economics. *Small* **2023**, *19* (39), e2303693. DOI: 10.1002/smll.202303693.
[28] Liu, X.; He, X.; Xiong, D.; Wang, G.; Tu, Z.; Wu, D.; Wang, J.; Gu, J.; Chen, Z. Electro-Reforming of PET Plastic to C2 Chemicals with Concurrent Generation of Hydrogen and Electric Energy. *ACS Catalysis* **2024**, *14* (7), 5366-5376. DOI: 10.1021/acscatal.4c00370.
[29] Xin, L.; Zhang, Z.; Qi, J.; Chadderdon, D.; Li, W. Electrocatalytic oxidation of ethylene glycol (EG) on supported Pt and Au catalysts in alkaline media: Reaction pathway investigation in three-electrode cell and fuel cell reactors. *Applied Catalysis B: Environmental* **2012**, *125*, 85-94. DOI: 10.1016/j.apcatb.2012.05.024.
[30] Wang, J.; Li, X.; Zhang, T.; Chen, Y.; Wang, T.; Zhao, Y. Electro-Reforming Polyethylene Terephthalate Plastic to Co-Produce Valued Chemicals and Green Hydrogen. *J Phys Chem Lett* **2022**, *13* (2), 622-627. DOI: 10.1021/acs.jpclett.1c03658.
[31] Shi, R.; Liu, K. S.; Liu, F.; Yang, X.; Hou, C. C.; Chen, Y. Electrocatalytic reforming of waste plastics into high value-added chemicals and hydrogen fuel. *Chem Commun (Camb)* **2021**, *57* (94), 12595-12598. DOI: 10.1039/d1cc05032j.
[32] Jiang, W.; Liu, J. K.; Zhou, H.; Huang, Z. J.; Wu, Y. X.; Cao, S.; Yang, D. X.; Wang, X. L.; Liu, P. F.; Zhou, Y. Operando *OH Tracking Unveils Heteroatom-Tailored Co3O4 Spinel Catalyst for Industrial-Level Current Density Ethylene Glycol Electrooxidation. *ACS Catalysis* **2025**, *15* (21), 18612-18622. DOI: 10.1021/acscatal.5c06358.
[33] Eppinger, J.; Huang, K.-W. Formic Acid as a Hydrogen Energy Carrier. *ACS Energy Letters* **2016**, *2* (1), 188-195. DOI: 10.1021/acsenergylett.6b00574.
[34] Overland, M.; Granli, T.; Kjos, N. P.; Fjetland, O.; Steien, S. H.; Stokstad, M. Effect of dietary formates on growth performance, carcass traits, sensory quality, intestinal microflora, and stomach alterations in growing-finishing pigs. *J Anim Sci* **2000**, *78* (7), 1875-1884. DOI: 10.2527/2000.7871875x (acccessed 6/2/2026).
[35] Song, M.; Wu, Y.; Zhao, Z.; Zheng, M.; Wang, C.; Lu, J. Corrosion Engineering of Part-Per-Million Single Atom Pt(1)/Ni(OH)(2) Electrocatalyst for PET Upcycling at Ampere-Level Current Density. *Adv Mater* **2024**, *36* (23), e2403234. DOI: 10.1002/adma.202403234.
[36] Du, D.; Liu, P.; Teng, Z.; Chen, T.; Zhu, J.; Shao, B.; Luo, J. Ampere-Level Upgrading of Polyethylene Terephthalate to Glycolate Using Palladium–Copper/Nickel Hydroxide Electrocatalysts. *ACS Catalysis* **2025**, *15* (4), 3038-3045. DOI: 10.1021/acscatal.4c07307.
[37] Ma, F.; Wang, S.; Gong, X.; Liu, X.; Wang, Z.; Wang, P.; Liu, Y.; Cheng, H.; Dai, Y.; Zheng, Z.; et al. Highly efficient electrocatalytic hydrogen evolution coupled with upcycling of microplastics in seawater enabled via Ni3N/W5N4 janus nanostructures. *Applied Catalysis B: Environment and Energy* **2022**, *307*. DOI: 10.1016/j.apcatb.2022.121198.
[38] Bajada, M. A.; Roy, S.; Warnan, J.; Abdiaziz, K.; Wagner, A.; Roessler, M. M.; Reisner, E. A Precious-Metal-Free Hybrid Electrolyzer for Alcohol Oxidation Coupled to CO(2) -to-Syngas Conversion. *Angew Chem Int Ed Engl* **2020**, *59* (36), 15633-15641. DOI: 10.1002/anie.202002680.
[39] Zhou, H.; Li, Z.; Xu, S. M.; Lu, L.; Xu, M.; Ji, K.; Ge, R.; Yan, Y.; Ma, L.; Kong, X.; et al. Selectively Upgrading Lignin Derivatives to Carboxylates through Electrochemical Oxidative C(OH)-C Bond Cleavage by a Mn-Doped Cobalt Oxyhydroxide Catalyst. *Angew Chem Int Ed Engl* **2021**, *60* (16), 8976-8982. DOI: 10.1002/anie.202015431.
[40] Liu, W. J.; Xu, Z.; Zhao, D.; Pan, X. Q.; Li, H. C.; Hu, X.; Fan, Z. Y.; Wang, W. K.; Zhao, G. H.; Jin, S.; et al. Efficient electrochemical production of glucaric acid and H(2) via glucose electrolysis. *Nat Commun* **2020**, *11* (1), 265. DOI: 10.1038/s41467-019-14157-3.
[41] Sherbo, R. S.; Delima, R. S.; Chiykowski, V. A.; MacLeod, B. P.; Berlinguette, C. P. Complete electron economy by pairing electrolysis with hydrogenation. *Nature Catalysis* **2018**, *1* (7), 501-507. DOI: 10.1038/s41929-018-0083-8.
[42] Zuo, Y.; Yu, D.; Zhang, X.; Wang, X. Electrocatalytic C horizontal line N Coupling in Aqueous Solutions for High-Value Product Synthesis. *Angew Chem Int Ed Engl* **2026**, *65* (14), e18370. DOI: 10.1002/anie.202518370.
[43] Wang, J.; Zhang, Z.; Liu, Y.; Wang, X.; Liu, M.; Quan, X.; Liu, Y. Inner-Axial Chlorine Engineering Enables Efficient and Selective Phenol Electrocatalytic Upcycling to Benzoquinone on Noble-Metal-Free Catalysts. *Angew Chem Int Ed Engl* **2026**, *65* (3), e21522. DOI: 10.1002/anie.202521522.
[44] Liu, D.; Zhu, Z.; Li, J.; Chen, L.-W.; Huang, H.-Z.; Jing, X.-T.; Yin, A.-X. Rh–Cu alloy nano-dendrites with enhanced electrocatalytic ethanol oxidation activity. *Journal of Energy Chemistry* **2023**, *82*, 343-349. DOI: 10.1016/j.jechem.2023.03.038.
[45] Zhao, C.-X.; Liu, J.-N.; Wang, C.; Wang, J.; Song, L.; Li, B.-Q.; Zhang, Q. An anionic regulation mechanism for the structural reconstruction of sulfide electrocatalysts under oxygen evolution conditions. *Energy & Environmental Science* **2022**, *15* (8), 3257-3264. DOI: 10.1039/d2ee01036d.
[46] Wang, Z.; Li, J.; Zhang, Q.; Wu, C.; Meng, H.; Tang, Y.; Zou, A.; Zhang, Y.; Ma, R.; Lv, X.; et al. Facilitating Formate Selectivity via Optimizing e(g)* Band Broadening in NiMn Hydroxides for Ethylene Glycol Electro-Oxidation. *Angew Chem Int Ed Engl* **2024**, *63* (44), e202411517. DOI: 10.1002/anie.202411517.
[47] Xiao, Z.; Guo, H.; Lv, F.; Lin, Z.; Sun, Z.; Sun, C.; Tan, Y.; Huang, Q.; Luo, M.; Guo, S. Geography-guided industrial-level upcycling of polyethylene terephthalate plastics through alkaline seawater-based processes. *Sci Adv* **2025**, *11* (22), eadu8381. DOI: 10.1126/sciadv.adu8381.
[48] Kang, S.; Yuan, W.; Guo, X.; Zhang, Y.; Shang, J.; Yang, P.; Ma, Y.; Nicolosi, V.; Cai, L.; Qiu, B. Concurrent Production of Glycolic Acid via Anode Valorization of Plastic Paired With Cathode Upcycling of Biomass Derivative. *Angew Chem Int Ed Engl* **2025**, *64* (30), e202504993. DOI: 10.1002/anie.202504993.
[49] Schwarzer, M.; Borodin, D.; Wang, Y.; Fingerhut, J.; Kitsopoulos, T. N.; Auerbach, D. J.; Guo, H.; Wodtke, A. M. Cooperative adsorbate binding catalyzes high-temperature hydrogen oxidation on palladium. *Science* **2024**, *386* (6721), 511-516. DOI: 10.1126/science.adk1334.
[50] Shi, R.; Wang, Y.; Chen, J.; Liu, F.; Sun, T.; Tse, E. C. M.; Chen, Y. Electrooxidation of Ethylene Glycol to Glycolic Acid in a Neutral Electrolyte via Enhanced *OH Generation and Directional Spillover. *Journal of the American Chemical Society* **2026**, *148* (9), 10216-10224. DOI: 10.1021/jacs.6c01709 (acccessed 9/2/2026).
[51] Liu, F.; Gao, X.; Shi, R.; Guo, Z.; Tse, E. C. M.; Chen, Y. Concerted and Selective Electrooxidation of Polyethylene-Terephthalate-Derived Alcohol to Glycolic Acid at an Industry-Level Current Density over a Pd-Ni(OH)(2) Catalyst. *Angew Chem Int Ed Engl* **2023**, *62* (11), e202300094. DOI: 10.1002/anie.202300094.
[52] Wang, H.; Dong, X.; Liu, F.; Chang, X.; Yu, T.; Chang, J.; Liu, M.; Zou, R.; Yang, Y.; Hou, C. C. Lattice-Distortion-Driven Electron Delocalization Enables Efficient Electrosynthesis of Glycolic Acid and Terephthalic Acid from Plastic Wastes. *J Am Chem Soc* **2026**, *148* (1), 1406-1418. DOI: 10.1021/jacs.5c17861.
[53] Liu, Y.; Hu, Z.; Zhu, X.; Li, X.; Zuo, T.; Zhao, Y.; Liu, G.; Cheng, Y.; Zhi, C.; Meng, J.; et al. Multimetallic Pt-Based Alloy Nanowires Library as a Platform for Selective Electrocatalytic Oxidation of Ethylene Glycol. *ACS Nano* **2026**, *20* (11), 9428-9439. DOI: 10.1021/acsnano.5c21597 (acccessed 9/2/2026).
[54] Liu, F.; Zhou, J.; Gao, X.; Shi, R.; Guo, Z.; Tse, E. C. M.; Chen, Y. Modulating Adsorption Behavior by Single-site Pt on RuO(2) for Efficient

Just Accepted

Electrosynthesis of Glycolic Acid from Plastic Wastes. *Angew Chem Int Ed Engl* **2025**, *64* (20), e202422183. DOI: 10.1002/anie.202422183.
[55] Si, D.; Xiong, B.; Chen, L.; Shi, J. Highly selective and efficient electrocatalytic synthesis of glycolic acid in coupling with hydrogen evolution. *Chem Catalysis* **2021**, *1* (4), 941-955. DOI: 10.1016/j.checat.2021.08.001.
[56] Shi, K.; Si, D.; Teng, X.; Chen, L.; Shi, J. Pd/NiMoO(4)/NF electrocatalysts for the efficient and ultra-stable synthesis and electrolyte-assisted extraction of glycolate. *Nat Commun* **2024**, *15* (1), 2899. DOI: 10.1038/s41467-024-47179-7.
[57] Zheng, Q.; Huang, L.; Yang, S.; Liang, Q.; Yang, Y.; Gu, L.; Cheng, R.; Shen, Y.; Yan, Z.; Cao, X. Synergy between multi-components and Ir dopant in Ir-doped high-entropy alloy nanoparticles for efficient and robust ethylene glycol electro-oxidation at an industrial-level current. *Nanoscale* **2025**, *17* (20), 12989-12999. DOI: 10.1039/d5nr00375j.
[58] Yue, S.; Zhao, Z.; Liu, Y.; Yang, M.; Zhang, T.; Li, F.; Liu, K.; Wang, P.; Zhan, S. Dual‐Site Synergistic Electrocatalysis Enables Highly Selective Upcycling of Real‐World Plastic Waste to Glycolic Acid. *Advanced Functional Materials* **2025**, *35* (49). DOI: 10.1002/adfm.202509766.
[59] Zhao, G.; Lin, J.; Lu, M.; Li, L.; Xu, P.; Liu, X.; Chen, L. Potential cycling boosts the electrochemical conversion of polyethylene terephthalate-derived alcohol into valuable chemicals. *Nat Commun* **2024**, *15* (1), 8463. DOI: 10.1038/s41467-024-52789-2.
[60] Lin, Y.; Chen, Y.; Ren, H.; Sun, Y.; Chen, J.; Wu, M.; Li, Z. Inspiration of Bimetallic Peroxide for Controllable Electrooxidizing Ethylene Glycol Through Modulating Surficial Intermediates. *Advanced Functional Materials* **2024**, *34* (42). DOI: 10.1002/adfm.202404594.
[61] Sun, Y.; Xie, Y.; Chen, X.; Wu, J.; Liu, P.; Wang, X.; Tian, Z.; Zheng, W.; Jiang, Z.; Kang, Z.; et al. Updating the sub-nanometric cognition of reconstructed oxyhydroxide active phase for water oxidation. *Nat Commun* **2025**, *16* (1), 3073. DOI: 10.1038/s41467-025-58424-y.
[62] Yang, C.; Gao, Y.; Wang, Y.; Cai, W.; Ma, J.; Zhang, J. Tailoring Coordination Microenvironment of Nickel Molecular Complexes for Electrooxidation of Organic Nucleophiles. *Angew Chem Int Ed Engl* **2025**, *64* (32), e202509377. DOI: 10.1002/anie.202509377.
[63] Li, J.; Li, L.; Ma, X.; Han, X.; Xing, C.; Qi, X.; He, R.; Arbiol, J.; Pan, H.; Zhao, J.; et al. Selective Ethylene Glycol Oxidation to Formate on Nickel Selenide with Simultaneous Evolution of Hydrogen. *Adv Sci (Weinh)* **2023**, *10* (15), e2300841. DOI: 10.1002/advs.202300841.
[64] Kang, H.; He, D.; Yan, X.; Dao, B.; Williams, N. B.; Elliott, G. I.; Streater, D.; Nyakuchena, J.; Huang, J.; Pan, X.; et al. Cu Promoted the Dynamic Evolution of Ni-Based Catalysts for Polyethylene Terephthalate Plastic Upcycling. *ACS Catal* **2024**, *14* (7), 5314-5325. DOI: 10.1021/acscatal.3c05509.
[65] Ma, Y.; Li, L.; Tang, J.; Hu, Z.; Zhang, Y.; Ge, H.; Jian, N.; Zhao, J.; Cabot, A.; Li, J. Electrochemical PET recycling to formate through ethylene glycol oxidation on Ni–Co–S nanosheet arrays. *Journal of Materials Chemistry A* **2024**, *12* (48), 33917-33925. DOI: 10.1039/d4ta07156e.
[66] Wang, N.; Li, X.; Hu, M.-K.; Wei, W.; Zhou, S.-H.; Wu, X.-T.; Zhu, Q.-L. Ordered macroporous superstructure of bifunctional cobalt phosphide with heteroatomic modification for paired hydrogen production and polyethylene terephthalate plastic recycling. *Applied Catalysis B: Environmental* **2022**, *316*. DOI: 10.1016/j.apcatb.2022.121667.
[67] Liu, X.; Fang, Z.; Xiong, D.; Gong, S.; Niu, Y.; Chen, W.; Chen, Z. Upcycling PET in parallel with energy-saving H2 production via bifunctional nickel-cobalt nitride nanosheets. *Nano Research* **2022**, *16* (4), 4625-4633. DOI: 10.1007/s12274-022-5085-9.
[68] Jiang, W.; Zhu, C.; Xu, H. G.; Liu, J. K.; Wu, Y. X.; Cao, S.; Yuan, H. Y.; Liu, P. F.; Zhou, Y. In situ reconstruction of Au promoted CuOOH/NiOOH for efficient and selective ethylene glycol electrooxidation. *Chemical Engineering Journal* **2025**, *515*. DOI: 10.1016/j.cej.2025.163804.
[69] Liu, J. K.; Kang, M.; Huang, K.; Xu, H. G.; Wu, Y. X.; Zhang, X. Y.; Zhu, Y.; Fan, H.; Fang, S. R.; Zhou, Y.; et al. Stable Ni(II) sites in Prussian blue analogue for selective, ampere-level ethylene glycol electrooxidation. *Nat Commun* **2025**, *16* (1), 3458. DOI: 10.1038/s41467-025-58203-9.
[70] Lu, X.; Guo, Y.; Liang, C.; Song, J.; Wu, Y.; Wang, Z.; Liu, Y.; Cheng, H.; Zheng, Z.; Huang, B.; et al. Alloying Strategy for the Electro-Upcycling of Polyethylene Terephthalate (PET) to C(2) Products at Industrial-Grade Current Density for over 700 h. *Small* **2025**, *21* (36), e05978. DOI: 10.1002/smll.202505978.
[71] Ma, F.; Zhang, C.; Li, W.; Hu, R.; Wang, Z.; Wang, J.; Li, J.; Nie, Y.; Zheng, Z.; Jiang, X. Selectively Steering the Retention and Cleavage of C–C Bond in Electrooxidation of PET Plastic and Biomass-Derived Alcohols by Defective Ni(OH)2–x-Supported Pt. *ACS Catalysis* **2025**, *15* (6), 4759-4769. DOI: 10.1021/acscatal.4c07644.
[72] Chen, Z.; Zheng, R.; Bao, T.; Ma, T.; Wei, W.; Shen, Y.; Ni, B.-J. Dual-Doped Nickel Sulfide for Electro-Upgrading Polyethylene Terephthalate into Valuable Chemicals and Hydrogen Fuel. *Nano-Micro Letters* **2023**, *15* (1), 210. DOI: 10.1007/s40820-023-01181-8.
[73] Liu, K.; Wang, Y.; Liu, F.; Liu, C.; Shi, R.; Chen, Y. Selective electrocatalytic reforming of PET-derived ethylene glycol to formate with a Faraday efficiency of 93.2% at industrial-level current densities. *Chemical Engineering Journal* **2023**, *473*, 145292. DOI: 10.1016/j.cej.2023.145292.
[74] Qin, Y.; Zhang, W.; Wang, F.; Li, J.; Ye, J.; Sheng, X.; Li, C.; Liang, X.; Liu, P.; Wang, X.; et al. Extraordinary p-d Hybridization Interaction in Heterostructural Pd-PdSe Nanosheets Boosts C-C Bond Cleavage of Ethylene Glycol Electrooxidation. *Angew Chem Int Ed Engl* **2022**, *61* (16), e202200899. DOI: 10.1002/anie.202200899.
[75] Liu, Y.; Wang, L.; Zhang, Y.; Xie, J.; Li, J.; Wei, J.; Zhang, M.; Yang, Y. From Ethylene Glycol to Glycolic Acid: Electrocatalytic Conversion on Pt-Group Metal Surfaces. *Inorg Chem* **2024**, *63* (31), 14794-14803. DOI: 10.1021/acs.inorgchem.4c02799.
[76] Cheng, J.; Tu, Y.; Xiang, Y.; Ni, J.; Guo, T.; Huang, X.; Liu, B.; Wei, Z. Anti-poisoning of CO and carbonyl species over Pd catalysts during the electrooxidation of ethylene glycol to glycolic acid at elevated current density. *Chem Sci* **2025**, *16* (10), 4303-4310. DOI: 10.1039/d4sc08579e.
[77] Sun, L.; Lv, H.; Xiao, J.; Liu, B. Enzymatic Mesoporous Metal Nanocavities for Concurrent Electrocatalysis of Nitrate to Ammonia Coupled with Polyethylene Terephthalate Upcycling. *Advanced Materials* **2024**, *36* (27), 2402767. DOI: 10.1002/adma.202402767 (acccessed 2026/09/03).
[78] Han, S.; Sun, L.; Fan, D.; Liu, B. Pulsed electrosynthesis of glycolic acid through polyethylene terephthalate upcycling over a mesoporous PdCu catalyst. *Nature Communications* **2025**, *16* (1), 3426. DOI: 10.1038/s41467-025-58813-3.
[79] Li, Y.; Yao, H.; Sun, L.; Han, S.; Xu, X.; Fan, G.; Liu, B. Trimetallic mesoporous PdCuRu for efficient formate electrosynthesis from polyethylene terephthalate recycling. *Science China Chemistry* **2025**, *68* (7), 3295-3301. DOI: 10.1007/s11426-024-2432-5.
[80] Zhang, Y.; Lin, Y.; Duan, T.; Song, L. Interfacial engineering of heterogeneous catalysts for electrocatalysis. *Materials Today* **2021**, *48*, 115-134. DOI: 10.1016/j.mattod.2021.02.004.
[81] Wang, C.; Bai, S.; Xiong, Y. Recent advances in surface and interface engineering for electrocatalysis. *Chinese Journal of Catalysis* **2015**, *36* (9), 1476-1493. DOI: 10.1016/s1872-2067(15)60911-1.
[82] Li, T.; Harrington, D. A. An Overview of Glycerol Electrooxidation Mechanisms on Pt, Pd and Au. *ChemSusChem* **2021**, *14* (6), 1472-1495. DOI: 10.1002/cssc.202002669.
[83] Ma, H.-Z.; He, S.-H.; Zhang, Y.; Wang, L.; Yi, Y.-N.; Yang, Y.-Y. Selective Electrocatalytic Oxidation of Ethylene Glycol into Glycolic Acid at Coin-Group Electrodes: An Investigation on Catalytic Activity and Selectivity. *ACS Sustainable Chemistry & Engineering* **2024**, *12* (32), 12249-12259. DOI: 10.1021/acssuschemeng.4c04928.
[84] Zhou, M.; Li, C.; Fang, J. Noble-Metal Based Random Alloy and Intermetallic Nanocrystals: Syntheses and Applications. *Chem Rev* **2021**, *121* (2), 736-795. DOI: 10.1021/acs.chemrev.0c00436.
[85] Crawley, J. W. M.; Gow, I. E.; Lawes, N.; Kowalec, I.; Kabalan, L.; Catlow, C. R. A.; Logsdail, A. J.; Taylor, S. H.; Dummer, N. F.; Hutchings, G. J. Heterogeneous Trimetallic Nanoparticles as Catalysts. *Chem Rev* **2022**, *122* (6), 6795-6849. DOI: 10.1021/acs.chemrev.1c00493.
[86] Bai, J.; Liu, D.; Yang, J.; Chen, Y. Nanocatalysts for Electrocatalytic Oxidation of Ethanol. *ChemSusChem* **2019**, *12* (10), 2117-2132. DOI: 10.1002/cssc.201803063.
[87] Fu, X.; Wan, C.; Huang, Y.; Duan, X. Noble Metal Based Electrocatalysts for Alcohol Oxidation Reactions in Alkaline Media. *Advanced Functional Materials* **2022**, *32* (11). DOI: 10.1002/adfm.202106401.
[88] Nakaya, Y.; Furukawa, S. Catalysis of Alloys: Classification, Principles, and Design for a Variety of Materials and Reactions. *Chem Rev* **2023**, *123* (9), 5859-5947. DOI: 10.1021/acs.chemrev.2c00356.
[89] Ma, Y.; Guo, X.; Du, M.; Kang, S.; Dong, W.; Nicolosi, V.; Cui, Z.; Zhang, Y.; Qiu, B. Beyond biodegradation: upcycling of polylactic acid plastic waste into amino acids via cascade catalysis under mild conditions. *Green Chemistry* **2024**, *26* (7), 3995-4004. DOI: 10.1039/d3gc04460b.
[90] Feng, F.; Han, S.; Ma, C.; Ma, X.; Lin, G.; Zhang, H.; He, C.; Jiao, X.; Meng, X.; Cao, W.; et al. Thiol‐Modulation‐Induced Mesoporous Nanosheets with an Alloy/Intermetallic Heterophase for Efficient Electrochemical Ethylene Glycol‐Assisted Water Splitting. *Advanced Functional Materials* **2025**, *35* (40). DOI: 10.1002/adfm.202506541.
[91] Zhao, J.; Chen, B.; Wang, F. Shedding Light on the Role of Misfit Strain in Controlling Core-Shell Nanocrystals. *Adv Mater* **2020**, *32* (46), e2004142. DOI: 10.1002/adma.202004142.
[92] Guo, H.; Guo, S. Strain Engineering of Multimetallic Nanomaterials for

Advanced Electrocatalysis. *CCS Chemistry* **2025**, *7* (2), 326-344. DOI: 10.31635/ccschem.024.202404677.
[93] Wang, C.; Zhang, J.; Miao, K.; Long, M.; Lai, S.; Zhao, S.; Kang, X. Octahedral Nanocrystals of Ru-Doped PtFeNiCuW/CNTs High-Entropy Alloy: High Performance Toward pH-Universal Hydrogen Evolution Reaction. *Adv Mater* **2024**, *36* (33), e2400433. DOI: 10.1002/adma.202400433.
[94] Lv, Y.; Lin, L.; Xue, R.; Zhang, P.; Ma, F.; Gan, T.; Zhang, J.; Gao, D.; Zheng, X.; Wang, L.; et al. Electronegativity Induced d‐Band Center Offset for Pt‐Rh Dual Sites in High‐Entropy Alloy Boosts Liquid Fuels Electrooxidation. *Advanced Energy Materials* **2024**, *14* (20). DOI: 10.1002/aenm.202304515.
[95] Fu, X.; Wan, C.; Huyan, H.; Wang, S.; Zhang, A.; Zhou, J.; Zhang, H.; Zhao, X.; Chen, J.; Pan, X.; et al. Medium entropy alloy wavy nanowires as highly effective and selective alcohol oxidation reaction catalysts for energy-saving hydrogen production and alcohol upgrade. *EES Catalysis* **2024**, *2* (6), 1285-1292. DOI: 10.1039/d4ey00090k.
[96] Wang, Y.; Luo, W.; Gong, S.; Luo, L.; Li, Y.; Zhao, Y.; Li, Z. Synthesis of High-Entropy-Alloy Nanoparticles by a Step-Alloying Strategy as a Superior Multifunctional Electrocatalyst. *Adv Mater* **2023**, *35* (36), e2302499. DOI: 10.1002/adma.202302499.
[97] Zhang, Y.; Wang, D.; Wang, S. High-Entropy Alloys for Electrocatalysis: Design, Characterization, and Applications. *Small* **2022**, *18* (7), e2104339. DOI: 10.1002/smll.202104339.
[98] Wu, Y.; Wang, X.; Kirlikovali, K. O.; Gong, X.; Atilgan, A.; Ma, K.; Schweitzer, N. M.; Gianneschi, N. C.; Li, Z.; Zhang, X.; et al. Catalytic Degradation of Polyethylene Terephthalate Using a Phase-Transitional Zirconium-Based Metal-Organic Framework. *Angew Chem Int Ed Engl* **2022**, *61* (24), e202117528. DOI: 10.1002/anie.202117528.
[99] Salciccioli, M.; Yu, W.; Barteau, M. A.; Chen, J. G.; Vlachos, D. G. Differentiation of O-H and C-H bond scission mechanisms of ethylene glycol on Pt and Ni/Pt using theory and isotopic labeling experiments. *J Am Chem Soc* **2011**, *133* (20), 7996-8004. DOI: 10.1021/ja201801t.
[100] Zhao, S.; Tan, C.; He, C.-T.; An, P.; Xie, F.; Jiang, S.; Zhu, Y.; Wu, K.-H.; Zhang, B.; Li, H.; et al. Structural transformation of highly active metal–organic framework electrocatalysts during the oxygen evolution reaction. *Nature Energy* **2020**, *5* (11), 881-890. DOI: 10.1038/s41560-020-00709-1.
[101] Dionigi, F.; Zeng, Z.; Sinev, I.; Merzdorf, T.; Deshpande, S.; Lopez, M. B.; Kunze, S.; Zegkinoglou, I.; Sarodnik, H.; Fan, D.; et al. In-situ structure and catalytic mechanism of NiFe and CoFe layered double hydroxides during oxygen evolution. *Nat Commun* **2020**, *11* (1), 2522. DOI: 10.1038/s41467-020-16237-1.
[102] Liu, L.; Corma, A. Structural transformations of solid electrocatalysts and photocatalysts. *Nat Rev Chem* **2021**, *5* (4), 256-276. DOI: 10.1038/s41570-021-00255-8.
[103] Martín, A. J.; Mitchell, S.; Mondelli, C.; Jaydev, S.; Pérez-Ramírez, J. Unifying views on catalyst deactivation. *Nature Catalysis* **2022**, *5* (10), 854-866. DOI: 10.1038/s41929-022-00842-y.
[104] Mefford, J. T.; Akbashev, A. R.; Kang, M.; Bentley, C. L.; Gent, W. E.; Deng, H. D.; Alsem, D. H.; Yu, Y. S.; Salmon, N. J.; Shapiro, D. A.; et al. Correlative operando microscopy of oxygen evolution electrocatalysts. *Nature* **2021**, *593* (7857), 67-73. DOI: 10.1038/s41586-021-03454-x.
[105] Huang, J.; Li, Y.; Zhang, Y.; Rao, G.; Wu, C.; Hu, Y.; Wang, X.; Lu, R.; Li, Y.; Xiong, J. Identification of Key Reversible Intermediates in Self-Reconstructed Nickel-Based Hybrid Electrocatalysts for Oxygen Evolution. *Angew Chem Int Ed Engl* **2019**, *58* (48), 17458-17464. DOI: 10.1002/anie.201910716.
[106] Li, S.; Ma, R.; Hu, J.; Li, Z.; Liu, L.; Wang, X.; Lu, Y.; Sterbinsky, G. E.; Liu, S.; Zheng, L.; et al. Coordination environment tuning of nickel sites by oxyanions to optimize methanol electro-oxidation activity. *Nat Commun* **2022**, *13* (1), 2916. DOI: 10.1038/s41467-022-30670-4.
[107] Qi, Y.; Zhang, Y.; Yang, L.; Zhao, Y.; Zhu, Y.; Jiang, H.; Li, C. Insights into the activity of nickel boride/nickel heterostructures for efficient methanol electrooxidation. *Nat Commun* **2022**, *13* (1), 4602. DOI: 10.1038/s41467-022-32443-5.
[108] Luo, H.; Yukuhiro, V. Y.; Fernandez, P. S.; Feng, J.; Thompson, P.; Rao, R. R.; Cai, R.; Favero, S.; Haigh, S. J.; Durrant, J. R.; et al. Role of Ni in PtNi Bimetallic Electrocatalysts for Hydrogen and Value-Added Chemicals Coproduction via Glycerol Electrooxidation. *ACS Catal* **2022**, *12* (23), 14492-14506. DOI: 10.1021/acscatal.2c03907.
[109] Liu, F.; Gao, X.; Shi, R.; Tse, E. C. M.; Chen, Y. A general electrochemical strategy for upcycling polyester plastics into added-value chemicals by a CuCo2O4 catalyst. *Green Chemistry* **2022**, *24* (17), 6571-6577. DOI: 10.1039/d2gc02049a.
[110] Li, C.; Sun, Y.; Li, Q.; Zhang, L.; Zhang, S.; Wang, H.; Hu, G.; Hu, X. Effects of volatiles on properties of char during sequential pyrolysis of PET and cellulose. *Renewable Energy* **2022**, *189*, 139-151. DOI: 10.1016/j.renene.2022.02.091.
[111] Evode, N.; Qamar, S. A.; Bilal, M.; Barceló, D.; Iqbal, H. M. N. Plastic waste and its management strategies for environmental sustainability. *Case Studies in Chemical and Environmental Engineering* **2021**, *4*, 100142. DOI: 10.1016/j.cscee.2021.100142.
[112] Chen, Z.; Wei, W.; Zou, W.; Li, J.; Zheng, R.; Wei, W.; Ni, B.-J.; Chen, H. Integrating electrodeposition with electrolysis for closed-loop resource utilization of battery industrial wastewater. *Green Chemistry* **2022**, *24* (8), 3208-3217. DOI: 10.1039/d1gc04891k.
[113] Chen, Z.; Zheng, R.; Graś, M.; Wei, W.; Lota, G.; Chen, H.; Ni, B.-J. Tuning electronic property and surface reconstruction of amorphous iron borides via W-P co-doping for highly efficient oxygen evolution. *Applied Catalysis B: Environmental* **2021**, *288*, 120037. DOI: 10.1016/j.apcatb.2021.120037.
[114] Kou, C.; Han, J.; Wang, H.; Han, M.; Liang, H. Unveiling the role of Zn dopants in NiFe phosphide nanosheet for oxygen evolution reaction. *Progress in Natural Science: Materials International* **2023**, *33* (1), 74-82. DOI: 10.1016/j.pnsc.2023.03.001.
[115] Wu, W.; Cao, Z.; Huai, A.; Long, Y.; Liu, H.; Xue, C.; Liu, D.; Huang, W. Potential-controlled electrocatalytic glycerol reforming over nickel-based conductive metal–organic framework for switchable formate and oxalate production. *Applied Surface Science* **2026**, *743*, 167314. DOI: 10.1016/j.apsusc.2026.167314.
[116] Yu, F.; Zhou, H.; Huang, Y.; Sun, J.; Qin, F.; Bao, J.; Goddard, W. A., 3rd; Chen, S.; Ren, Z. High-performance bifunctional porous non-noble metal phosphide catalyst for overall water splitting. *Nat Commun* **2018**, *9* (1), 2551. DOI: 10.1038/s41467-018-04746-z.
[117] Lin, C.-Y.; Huang, S.-C.; Lin, Y.-G.; Hsu, L.-C.; Yi, C.-T. Electrosynthesized Ni-P nanospheres with high activity and selectivity towards photoelectrochemical plastics reforming. *Applied Catalysis B: Environmental* **2021**, *296*. DOI: 10.1016/j.apcatb.2021.120351.
[118] Yang, S.; Zhu, J.-Y.; Chen, X.-N.; Huang, M.-J.; Cai, S.-H.; Han, J.-Y.; Li, J.-S. Self-supported bimetallic phosphides with artificial heterointerfaces for enhanced electrochemical water splitting. *Applied Catalysis B: Environmental* **2022**, *304*. DOI: 10.1016/j.apcatb.2021.120914.
[119] Chen, M. T.; Duan, J. J.; Feng, J. J.; Mei, L. P.; Jiao, Y.; Zhang, L.; Wang, A. J. Iron, rhodium-codoped Ni(2)P nanosheets arrays supported on nickel foam as an efficient bifunctional electrocatalyst for overall water splitting. *J Colloid Interface Sci* **2022**, *605*, 888-896. DOI: 10.1016/j.jcis.2021.07.101.
[120] Chai, L.; Hu, Z.; Wang, X.; Xu, Y.; Zhang, L.; Li, T. T.; Hu, Y.; Qian, J.; Huang, S. Stringing Bimetallic Metal-Organic Framework-Derived Cobalt Phosphide Composite for High-Efficiency Overall Water Splitting. *Adv Sci (Weinh)* **2020**, *7* (5), 1903195. DOI: 10.1002/advs.201903195.
[121] Zhao, Y.; Dongfang, N.; Triana, C. A.; Huang, C.; Erni, R.; Wan, W.; Li, J.; Stoian, D.; Pan, L.; Zhang, P.; et al. Dynamics and control of active sites in hierarchically nanostructured cobalt phosphide/chalcogenide-based electrocatalysts for water splitting. *Energy Environ Sci* **2022**, *15* (2), 727-739. DOI: 10.1039/d1ee02249k.
[122] Liu, M.; Pang, Y.; Zhang, B.; De Luna, P.; Voznyy, O.; Xu, J.; Zheng, X.; Dinh, C. T.; Fan, F.; Cao, C.; et al. Enhanced electrocatalytic CO(2) reduction via field-induced reagent concentration. *Nature* **2016**, *537* (7620), 382-386. DOI: 10.1038/nature19060.
[123] Yang, C. L.; Wang, L. N.; Yin, P.; Liu, J.; Chen, M. X.; Yan, Q. Q.; Wang, Z. S.; Xu, S. L.; Chu, S. Q.; Cui, C.; et al. Sulfur-anchoring synthesis of platinum intermetallic nanoparticle catalysts for fuel cells. *Science* **2021**, *374* (6566), 459-464. DOI: 10.1126/science.abj9980.
[124] Zhu, Y.; Chen, S.; Zou, J.; Li, B.; Ren, W.; Zhang, G.; Wang, J.; Liu, X.; Li, Q.; Zhang, H.; et al. Single-atom catalysts partner with defects to open a new chapter in catalysis: Synthesis, performances, and mechanisms. *Chinese Chemical Letters* **2026**, *37* (7). DOI: 10.1016/j.cclet.2025.112192.
[125] Wang, A.; Li, J.; Zhang, T. Heterogeneous single-atom catalysis. *Nature Reviews Chemistry* **2018**, *2* (6), 65-81. DOI: 10.1038/s41570-018-0010-1.
[126] Wang, Y.; Su, H.; He, Y.; Li, L.; Zhu, S.; Shen, H.; Xie, P.; Fu, X.; Zhou, G.; Feng, C.; et al. Advanced Electrocatalysts with Single-Metal-Atom Active Sites. *Chem Rev* **2020**, *120* (21), 12217-12314. DOI: 10.1021/acs.chemrev.0c00594.
[127] Li, Z.; Ji, S.; Liu, Y.; Cao, X.; Tian, S.; Chen, Y.; Niu, Z.; Li, Y. Well-Defined Materials for Heterogeneous Catalysis: From Nanoparticles to Isolated Single-Atom Sites. *Chem Rev* **2020**, *120* (2), 623-682. DOI: 10.1021/acs.chemrev.9b00311.
[128] Chen, W.; Shi, J.; Wu, Y.; Jiang, Y.; Huang, Y. C.; Zhou, W.; Liu, J.; Dong, C. L.; Zou, Y.; Wang, S. Vacancy-induced catalytic mechanism for alcohol electrooxidation on nickel-based electrocatalyst. *Angew Chem Int Ed Engl* **2024**, *63* (4), e202316449. DOI: 10.1002/anie.202316449.
[129] Jie Hu, D. J., Zhaoyue Weng, Ying Pan, Zhongjun Li, Haiwei Du,

In Accepted

Yupeng Yuan,. A universal electrochemical activation enabling lattice oxygen activation in nickel-based catalyst for efficient water oxidation. *Chemical Engineering Journal* **2022**. DOI: 10.1016/j.cej.2021.132736.
[130] Li, J.; Lian, R.; Wang, J.; He, S.; Jiang, S. P.; Rui, Z. Oxygen vacancy defects modulated electrocatalytic activity of iron-nickel layered double hydroxide on Ni foam as highly active electrodes for oxygen evolution reaction. *Electrochimica Acta* **2020**, *331*. DOI: 10.1016/j.electacta.2019.135395.
[131] Xiang, Q.; Chen, F.; Zhou, Y.; Pan, X.; Zhu, H. Phosphorus doping in high-entropy carbides promotes the selectivity in electrooxidation of ethylene glycol to formic acid. *New Journal of Chemistry* **2025**, *49* (18), 7553-7559. DOI: 10.1039/d5nj00129c.
[132] Bolar, S.; Ito, A.; Yuan, C.; Wang, M.; Yamaguchi, A.; Miyauchi, M.; Fujita, T. Sulfur-Stabilized High Entropy Oxysulfides Enable Efficient C C Bond Cleavage in Ethylene Glycol Electrooxidation for Sustainable Plastic Upcycling to Formate. *ChemSusChem* **2026**, *19* (5), e202502529. DOI: 10.1002/cssc.202502529.
[133] Chen, W.; Zhang, L.; Xu, L.; He, Y.; Pang, H.; Wang, S.; Zou, Y. Pulse potential mediated selectivity for the electrocatalytic oxidation of glycerol to glyceric acid. *Nat Commun* **2024**, *15* (1), 2420. DOI: 10.1038/s41467-024-46752-4.
[134] Wang, L.; Meng, H.; Shen, P. K.; Bianchini, C.; Vizza, F.; Wei, Z. In situ FTIR spectroelectrochemical study on the mechanism of ethylene glycol electrocatalytic oxidation at a Pd electrode. *Phys Chem Chem Phys* **2011**, *13* (7), 2667-2673. DOI: 10.1039/c0cp01913e (acccessed 7/19/2026).
[135] Wang, H.; Jiang, B.; Zhao, T.-T.; Jiang, K.; Yang, Y.-Y.; Zhang, J.; Xie, Z.; Cai, W.-B. Electrocatalysis of Ethylene Glycol Oxidation on Bare and Bi-Modified Pd Concave Nanocubes in Alkaline Solution: An Interfacial Infrared Spectroscopic Investigation. *ACS Catalysis* **2017**, *7* (3), 2033-2041. DOI: 10.1021/acscatal.6b03108.
[136] Schnaidt, J.; Heinen, M.; Jusys, Z.; Behm, R. J. Electro-Oxidation of Ethylene Glycol on a Pt-Film Electrode Studied by Combined in Situ Infrared Spectroscopy and Online Mass Spectrometry. *The Journal of Physical Chemistry C* **2012**, *116* (4), 2872-2883. DOI: 10.1021/jp208162q.
[137] Brummel, O.; Lykhach, Y.; Ralaiarisoa, M.; Berasategui, M.; Kastenmeier, M.; Fusek, L.; Simanenko, A.; Gu, W.; Clark, P. C. J.; Yivlialin, R.; et al. A Versatile Approach to Electrochemical In Situ Ambient-Pressure X-ray Photoelectron Spectroscopy: Application to a Complex Model Catalyst. *J Phys Chem Lett* **2022**, *13* (47), 11015-11022. DOI: 10.1021/acs.jpclett.2c03004.
[138] Zhou, L.; Sun, Y.; Wu, Y.; Zhu, Y.; Xu, Y.; Jia, J.; Wang, F.; Wang, R. Controlled Growth of Pd Nanocrystals by Interface Interaction on Monolayer MoS(2): An Atom-Resolved in Situ Study. *Nano Lett* **2023**, *23* (23), 11360-11367. DOI: 10.1021/acs.nanolett.3c03960.
[139] Rojas-Luna, R. l.; Cousins, L. S.; Germaney, R.; Gil-Gavilán, D. G.; Castillo-Rodríguez, M.; Garcia Osorio, D.-A.; Doughty, T.; Esquivel, D.; Creissen, C. E.; Roy, S. Coelectrolysis of PET and CO2 Using an Electrochemically Restructured Co-MOF-74 Anode and a Polymeric Co-Phthalocyanine Cathode. *ACS Applied Materials & Interfaces* **2026**, *18* (4), 6937-6951. DOI: 10.1021/acsami.5c22269 (acccessed 9/2/2026).
[140] Yu, X.; Rabiee, H.; Dutta, A.; Li, Y.; Szakály, Z.; Vesztergom, S.; Warmuth, L.; Rieder, A.; Broekmann, P. Upcycling CO2 and PET Waste: Ampere-Level Formate Electrosynthesis in an Integrated Electrolyzer. *Journal of the American Chemical Society* **2025**, *147* (45), 41481-41491. DOI: 10.1021/jacs.5c11708 (acccessed 9/2/2026).
[141] Wang, Z.; Xue, Z.; Fan, D.; Jiang, J.; Hao, Q.; Xiang, X.; Shan, Y.; Xu, D.; Chen, L.; Liu, B. Ultrathin AuCu Nanodendrites for Efficient Ethylene Glycol Electrooxidation. *ChemistryEurope* **2026**, *4* (3), e202500491. DOI: 10.1002/ceur.202500491 (acccessed 2026/09/02).
[142] Reshma, C. S.; Remya, S.; Bindu, J. A review of exploring the synthesis, properties, and diverse applications of poly lactic acid with a focus on food packaging application. *International Journal of Biological Macromolecules* **2024**, *283*, 137905. DOI: 10.1016/j.ijbiomac.2024.137905.
[143] Sato, S. Application of Glyceric Acid to Bio-related Functional Materials and Improvement of Microbial Production. *J Oleo Sci* **2021**, *70* (3), 289-295. DOI: 10.5650/jos.ess20307.
[144] Liu, D.; Liu, J.-C.; Cai, W.; Ma, J.; Yang, H. B.; Xiao, H.; Li, J.; Xiong, Y.; Huang, Y.; Liu, B. Selective photoelectrochemical oxidation of glycerol to high value-added dihydroxyacetone. *Nature Communications* **2019**, *10* (1), 1779. DOI: 10.1038/s41467-019-09788-5.
[145] Han, S.; Liu, B. Robust Formate Electrosynthesis from Mixed Biomass Polyols by a Direct Carbon–Carbon Bond Cleavage Route. *Journal of the American Chemical Society* **2025**, *148* (1), 778-789. DOI: 10.1021/jacs.5c16299 (acccessed 9/3/2026).
[146] Liu, P.; Tang, D.; Han, S.; Qiao, Z.-A.; Liu, B. Mesoporous Anti-Perovskite CuNi3N for Sustainable Formate Electrosynthesis from Complete Electrooxidation of Biomass Glucose. *Angewandte Chemie International Edition* **2026**, *65* (30), e7507967. DOI: 10.1002/anie.7507967 (acccessed 2026/09/03).
[147] Ma, Z.; Cui, P.; Wang, X.; Li, L.; Xu, H.; Fisher, A.; Cheng, D. The integration of artificial intelligence and high-throughput experiments: An innovative driving force in catalyst design. *Chinese Journal of Chemical Engineering* **2025**, *84*, 117-132. DOI: 10.1016/j.cjche.2025.04.012.
[148] Canty, R. B.; Abolhasani, M. Reproducibility in automated chemistry laboratories using computer science abstractions. *Nature Synthesis* **2024**, *3* (11), 1327-1339. DOI: 10.1038/s44160-024-00649-8.
[149] Pendleton, I. M.; Cattabriga, G.; Li, Z.; Najeeb, M. A.; Friedler, S. A.; Norquist, A. J.; Chan, E. M.; Schrier, J. Experiment Specification, Capture and Laboratory Automation Technology (ESCALATE): a software pipeline for automated chemical experimentation and data management. *MRS Communications* **2019**, *9* (3), 846-859. DOI: 10.1557/mrc.2019.72.
[150] Tom, G.; Schmid, S. P.; Baird, S. G.; Cao, Y.; Darvish, K.; Hao, H.; Lo, S.; Pablo-Garcia, S.; Rajaonson, E. M.; Skreta, M.; et al. Self-Driving Laboratories for Chemistry and Materials Science. *Chem Rev* **2024**, *124* (16), 9633-9732. DOI: 10.1021/acs.chemrev.4c00055.
[151] Timoshenko, J.; Haase, F. T.; Saddeler, S.; Rüscher, M.; Jeon, H. S.; Herzog, A.; Hejral, U.; Bergmann, A.; Schulz, S.; Roldan Cuenya, B. Deciphering the Structural and Chemical Transformations of Oxide Catalysts during Oxygen Evolution Reaction Using Quick X‐ ray Absorption Spectroscopy and Machine Learning. *Journal of the American Chemical Society* **2023**, *145* (7), 4065-4080. DOI: 10.1021/jacs.2c11824 (acccessed 9/8/2026).
[152] Martini, A.; Timoshenko, J.; Grosse, P.; Rettenmaier, C.; Hursán, D.; Deplano, G.; Jeon, H. S.; Bergmann, A.; Roldan Cuenya, B. Adsorbate Configurations in Ni Single-Atom Catalysts during ${\mathrm{CO}}_{2}$ Electrocatalytic Reduction Unveiled by Operando XAS, XES, and Machine Learning. *Physical Review Letters* **2024**, *133* (22), 228001. DOI: 10.1103/PhysRevLett.133.228001.
[153] Hlophe, P. V.; Tawalbeh, M.; Al-Othman, A.; Msomi, P. F. Autonomous AI agents in ORR electrocatalyst discovery: a review of closed-loop workflows, materials bottlenecks, and energy system translation. *Materials Advances* **2026**, *7* (13), 6474-6485. DOI: 10.1039/d6ma00429f (acccessed 9/8/2026).
[154] Li, J.; Lu, X.; Chen, Y.; Zhong, Y.; Yao, J.; Wang, J.; Wang, X. Machine learning-guided high-throughput screening of dual-atom catalysts for electrochemical C-C coupling. *Chemical Engineering Science* **2026**, *320*. DOI: 10.1016/j.ces.2025.122415.
[155] Cheng, P.; Xu, H.; Wang, X.; Wang, X.; Wang, T.; Yu, C.; Sun, W.; Li, Y.; Huang, W.; Chen, C. Accelerated discovery of M6@g-N4 catalysts for CO2 electroreduction via machine learning and DFT: descriptor engineering and activity trend validation. *Phys Chem Chem Phys* **2026**, *28* (21), 12876-12886. DOI: 10.1039/d6cp00864j (acccessed 7/21/2026).
[156] Xu, W.; Diesen, E.; He, T.; Reuter, K.; Margraf, J. T. Discovering High Entropy Alloy Electrocatalysts in Vast Composition Spaces with Multiobjective Optimization. *J Am Chem Soc* **2024**, *146* (11), 7698-7707. DOI: 10.1021/jacs.3c14486.
[157] Li, X.; Chiong, R.; Hu, Z.; Page, A. J. A graph neural network model with local environment pooling for predicting adsorption energies. *Computational and Theoretical Chemistry* **2023**, *1226*. DOI: 10.1016/j.comptc.2023.114161.

Under Review